The Level Set Ensemble Kalman Filter: Sequential Data Assimilation for Flows With Shocks

Michael K. Sleeman[a,*], Lorenzo Beronilla[b], Hangchuan Hu[c], Xu-Hui Zhou[b,a], Matthias Morzfeld[b], Andrew M. Stuart[a], Tamer A. Zaki[c]

[a] *Computing + Mathematical Sciences, California Institute of Technology, Pasadena, 91125, CA, USA*
[b] *Scripps Institution of Oceanography, University of California San Diego, La Jolla, 92093, CA, USA*
[c] *Department of Mechanical Engineering, Johns Hopkins University, Baltimore, 21218, MD, USA*

Abstract

The ensemble Kalman filter is commonly used to perform sequential data assimilation in science and engineering because of its robust performance and scalability when the state space dimension is high. However, the standard EnKF generates spurious oscillations when applied to compressible flows with shocks; the cause is the uncertainty, across the ensemble, in the shock location. This paper develops the *level set EnKF*, which overcomes this challenge by employing a nonlinear mapping from the original state space into a latent space in which the analysis step is undertaken. The latent representation comprises a level set function that encodes the discontinuity location and smooth state extensions, defined over the full physical domain, that represent the solution on either side of the discontinuity. We first formulate the level set EnKF as a specific instance of a more general approach of performing data assimilation in a latent space. We then demonstrate the feasibility of the level set EnKF for several one-dimensional compressible flows and a two-dimensional blast wave.

Keywords: data assimilation, ensemble Kalman filter, shocks, shock detection, discontinuities, level set.

1. Introduction

1.1. Goal

Sequential and variational data assimilation (DA) methods have proved successful at combining predicted partial differential equation (PDE) models with partial, noisy observations, to improve state estimates and enable uncertainty quantification. However, many standard methods for large-scale problems fail in the presence of shocks and other discontinuities [1, 2, 3]. In this paper, we consider ensemble-based sequential DA for compressible flows with sharp discontinuities (i.e., shocks and contact surfaces). We present a general

*Corresponding author.
Email address: msleeman@caltech.edu (Michael K. Sleeman)

framework in which the analysis step is applied in a latent space, rather than the original state space, to address the failure modes of standard ensemble methods near discontinuities.

We then develop a specific implementation of this framework, which we term the *level set EnKF*. The method relies on three key ingredients: (i) hyperbolic tangent profiles to model numerically smeared discontinuities, (ii) gradient-based detection of candidate discontinuity locations, and (iii) a nonlinear least-squares optimization to identify the *level set representation*. These three ingredients together result in a latent[1] representation in terms of a level set function, which encodes discontinuity location, and smooth state extensions, from either side of the discontinuity, defined everywhere on the physical domain. We demonstrate that performing the analysis step of EnKF in the resulting latent space preserves sharp discontinuities. The approach is illustrated for several one-dimensional (1D) compressible flows and for a two-dimensional (2D) blast wave problem.

1.2. Literature Review and Context

Physical phenomena can be investigated through a combination of observation and mathematical modeling. Sensors provide physically grounded measurements but are inherently limited by noise, finite spatio-temporal resolution, and incomplete observability. In contrast, mathematical models based on PDEs, when discretized and solved numerically, provide access to the complete state at arbitrary resolution, but at the expense of errors, for example in the initial and boundary conditions. DA offers a principled framework to combine models and data to obtain improved state estimates [4] and to perform uncertainty quantification [5]. It has been applied to diverse fields of science and engineering, including weather forecasting [6], turbulence modeling [7], oil reservoir simulation [8] and other problems in the geophysical sciences [9]. More recently, DA has been increasingly applied to flow estimation and prediction in fluid mechanics [10, 11, 12, 13, 14, 15, 16]. While much of this work has focused on incompressible and smoothly varying flows, there is growing interest in DA for high-speed compressible flows [17, 18, 19, 20] and for flows containing shocks and other discontinuities [1, 2, 3].

We first review sequential DA methods for compressible flows and other problems with discontinuities in Subsubsection 1.2.1. We then review methods for shock detection in Subsubsection 1.2.2 and recent work on hyperbolic tangent representations of discontinuities in Subsubsection 1.2.3; these topics are relevant because the proposed method requires that discontinuities be detected explicitly, and we choose to model discontinuities using the hyperbolic tangent function.

[1] The level set representation is higher dimensional than the physical space representation, but a latent representation need not reduce the dimension of the state; generally latent spaces are sought, in many areas of science and engineering, to identify a space in which computations may be performed favorably because, in some relevant topology, points are close together in the latent space. The level set representation for shocks enables the EnKF analysis update to preserve sharp features present in the forecast ensemble.

1.2.1. Sequential DA for Compressible Flows

The *filtering distribution* is defined through an iterative Bayesian framework: model *prediction* using the underlying PDE provides a prior distribution; this prior information is updated using observational data to obtain a posterior prediction in what is known as the *analysis*; the process of prediction and analysis is cycled to incorporate observations sequentially in time. Filtering algorithms, or simply filters, refer to a class of sequential DA algorithms designed to approximate the filtering distribution. Here we study filters for compressible flows modeled by the compressible Euler equations (see Appendix A), whose solutions contain shocks and contact surfaces.

The bootstrap particle filter (PF) [21, 22, 23] employs a set of weighted particles to approximate the filtering distribution; it applies quite generally and, in particular, converges to the true filtering distribution, in the large particle limit, without making any Gaussian assumptions. However, the method suffers from *weight collapse* in which all but one particle carry negligible weights. This issue is particularly pronounced for problems in which the state space dimension is high [24, 25], such as the spatially discretized Euler equations. As a consequence, the ensemble Kalman filter (EnKF) [4, 26], which works with equally weighted ensemble members, is widely used in high dimensional settings. However, the EnKF is most effective when uncertainties are well approximated by Gaussian distributions. This assumption is problematic for compressible flows with shocks: when the shock location is uncertain, the state distribution at a fixed spatial location within the range of possible shock locations can become bimodal, since different ensemble members may place that location on different sides of the shock [3]. The EnKF analysis step can then mix pre- and post-shock states, producing nonphysical oscillations near the discontinuity, as observed by Houba *et al.* [1] for 1D shock propagation problems.

Houba *et al.* [1] show that the PF preserves shocks in compressible flows, provided that all forecast states contain the same number of shocks. However, weight collapse remains a problem in general. To mitigate this issue, Subrahmanya and Sandu [27] combine the Ensemble Transform Particle Filter (ETPF) [28] with *dynamic time warping* (DTW) [29] to align features when taking convex combinations of particles. They further employ underweighting (i.e., inflation of the assumed observation-error covariance), to delay weight collapse.

Despite this body of work, weight collapse remains a limitation of particle-filter-based methods, motivating the development of EnKF-based approaches for filtering problems with discontinuities. Recent work by Edoh *et al.* [2] applied the EnKF to transformed variables to enforce positivity, although this transformation does not address the spurious oscillations caused by misaligned discontinuities. More recently, several methods have instead applied the EnKF in a latent space. Zhou *et al.* [3] developed the *neural EnKF*, which represents the state using the weights and biases of a neural network and performs DA in this latent space. Chandravamsi *et al.* [30] similarly learn a shared decoder that maps latent variables to the physical state and perform DA in the learned latent space. The *morphing EnKF* of Beezley and Mandel [31] instead constructs a latent space using image registration [32], comprising an invertible registration map together with the aligned state. Originally developed for wildfire forecasting, it has recently been extended to compressible flows [33].

The DA approaches above illustrate how performing the EnKF step in a latent space yields an improved analysis step for fields with discontinuities. This principle has also been explored for inverse problems by Chada *et al.* [34], who used level set based latent space to solve inverse problems with ensemble Kalman inversion (EKI). That paper deploys the level set methodology to reconstruct piecewise constant and piecewise continuous fields. Their parameterization is related to the level set representation that we develop in Section 3. Implementing the resulting inversion methodology requires only a map from the latent space to physical space, which is straightforward. In contrast, the present work addresses a sequential filtering problem and therefore requires repeated interaction with the PDE solver. Consequently, it also requires a map from physical space to latent space, which is considerably more challenging. The present work develops efficient tools for doing so.

1.2.2. Shock Detection

Shocks and contact surfaces have a finite width, but this width is small compared to macroscopic flow scales, and they can be idealized to have infinitesimal width [35]. However, numerical solutions to the compressible Euler equations smear shocks and contact surfaces over multiple cells [36], which makes it challenging to precisely identify locations of discontinuities. Here, we review methods for detecting shocks and contact surfaces.

Shock-capturing methods solve hyperbolic conservation laws, such as the Euler equations, while allowing shocks and other discontinuities to form without explicitly tracking their locations. They use numerical dissipation to spread discontinuities over a few grid cells and suppress spurious oscillations [36]. This dissipation may be introduced through artificial viscosity [37], but is more commonly built into Godunov-type schemes, including *monotonic upstream-centered schemes for conservation laws* (MUSCL) [38] and *weighted essentially non-oscillatory* (WENO) methods [39]. We refer to Appendix A and Toro [36] for a more detailed treatment of shock-capturing methods for the Euler equations.

Although shock-capturing methods do not explicitly track discontinuities, many schemes that rely on artificial diffusion use *shock sensors*[2] to adaptively increase artificial diffusion in regions with large solution gradients. Jameson *et al.* [40] introduced an adaptive artificial viscosity method based on a pressure sensor, Ducros *et al.* [41] developed a related sensor based on the velocity field, and Moro *et al.* [42] later proposed a dilation-based shock sensor. Despite their widespread use for controlling artificial dissipation, shock sensors have been used less often for explicit detection of shock location. We note, however, that Razavi and Yano [43] used the dilation-based sensor of Moro *et al.* to locate shocks.

Wu *et al.* [44] reviewed methods for shock detection, including the *Normal Mach number* approach of Lovely and Haimes [45] and the characteristic-based approach of Kanamori and Suzuki [46]. More recent methods have used image-processing and machine-learning techniques: Fujimoto *et al.* [47] used Canny edge detection [48], Liu *et al.* [49] developed a convolutional neural network (CNN)-based shock detector, and Chang *et al.* [50] developed a

[2]Here, a *shock sensor* refers to a numerical method used to identify regions containing shocks or other sharp discontinuities, rather than a physical measurement device.

cluster-analysis method to detect shocks. The proposed level set representation method (see Section 3) can be adapted to employ any future improvements in robust shock detection.

1.2.3. Modeling Sharp Gradients Using Hyperbolic Tangent Profiles

In the present work, shocks and contact surfaces are represented using hyperbolic tangent profiles. This representation is related to the tangent of hyperbola for interface capturing (THINC) method introduced by Xiao *et al.* [51], in which hyperbolic-tangent profiles are used to capture moving interfaces in multi-fluid simulations. Baumgart *et al.* [52] similarly represented shocks using hyperbolic tangent profiles and estimated the profile parameters through least-squares regression; the present work employs a similar approach.

Although THINC was not originally developed to sharpen numerically smeared discontinuities, Fukushima and Kitamura [53] applied it to discontinuities smeared by MUSCL schemes. They found that the method sharpened contact surfaces and weak shocks without introducing numerical oscillations, whereas sharpening strong shocks produced spurious oscillations. We explore using our hyperbolic tangent representation to sharpen shocks in Appendix B, and we find that doing so leads to oscillations. Therefore, we sharpen only contact surfaces. More generally, numerical solutions of the Euler equations introduce an intrinsic length scale associated with the width of a shock, and we seek a level set representation that preserves this scale.

1.3. Numerical Solutions of the Euler Equations

In this work, we model compressible flows using the Euler equations, as outlined in Appendix A. We solve these equations numerically using the open-source solver `M2C` (Multiphysics Modeling and Computation) [54], which implements a MUSCL scheme [38]. We compute numerical fluxes using a local Lax-Friedrichs approximate Riemann solver and integrate in time using an explicit second-order Runge-Kutta scheme. We refer to Toro [36] for more details on compressible flow solvers. Throughout this work, all level set representations and level set EnKF updates are constructed from cell-centered solution values.

1.4. Latent Space EnKF and the Level Set Representation

The neural-network-based approaches of Zhou *et al.* [3] and Chandravamsi *et al.* [30] perform the EnKF in a learned latent space rather than directly in the physical state space. Similarly, the morphing EnKF [31] defines a latent space consisting of a registration map and the corresponding aligned state representation. In this work, we present a general framework for latent-space EnKF methods, of which these approaches are specific instances.

A suitable transformation to latent space should satisfy three properties:

1. its inverse should accurately reconstruct the physical state;
2. its inverse should be *feature-preserving*; and
3. the latent representation should vary smoothly across ensemble members.

The first property limits reconstruction error, while the second ensures that latent space perturbations preserve sharp physical features, such as shocks. The third makes the latent space more amenable to the linear combinations performed by the EnKF.

In the level set EnKF, level set functions encode discontinuity locations through their zero level sets, while smooth state extensions represent the solution on either side of each discontinuity. This representation is designed to satisfy the criteria above: reconstructing from the latent variables preserves sharp discontinuities, and separating discontinuity locations from smooth state values yields latent variables that vary smoothly across ensemble members.

1.5. Contributions and Paper Outline

The primary contribution of this paper is the development of the *level set representation* and its application to feature-preserving DA for systems with discontinuities via the *level set EnKF*. We show that the method performs well for 1D and 2D compressible Euler problems with uncertain shock locations. Beyond its application to DA, the level set representation could also be used to extract shock properties from CFD data. In particular, the representation yields the shock location and state values on either side of the shock, allowing the shock strength and propagation speed to be computed. Conversely, advances in shock-detection methods could improve future implementations of the level set representation. A secondary contribution is that we present a general framework for latent space EnKF; we place the level set methodology in this framework and highlight that the existing neural-network-based methods [3, 30], and the morphing EnKF [31], are specific instances of this framework.

Section 2 introduces the notations for the standard and transformed EnKFs. Section 3 develops the level set representation for 1D scalar fields with one or more discontinuities, while Section 4 demonstrates its application to solve data assimilation problems arising in the 1D Euler equations. In particular Section 4 demonstrates the level set EnKF for the 1D compressible Euler equations by applying it to Toro's shock tube problem [36], the Shu-Osher shock-entropy problem [55], and Sod's shock tube problem [56]. Section 5 extends the level set representation so that it may be used to enable DA for solutions of the 2D Euler equations; and we illustrate the methodology when applied to data assimilation for the blast wave problem investigated in [27]. We conclude in Section 6.

2. EnKF and Discontinuous Flow Fields

We first review the standard EnKF in Subsection 2.1. We then introduce the transformed EnKF in Subsection 2.2, discuss methods to construct appropriate latent space transformation in Subsection 2.3, and demonstrate the transformed EnKF for a hyperbolic tangent profile in Subsection 2.4.

2.1. Standard EnKF

Consider a discretized physical state $\boldsymbol{z}_j \in \mathbb{R}^{N_z}$ at observation times t_j for $j = 1, \ldots, J$ [3]. Let operator $\mathcal{P} : \mathbb{R}^{N_z} \to \mathbb{R}^{N_z}$ advance the state between observation times, assuming that

[3]For ease of exposition we assume that these times are equally spaced, but this assumption is readily dispensed with in what follows.

this is defined by a (discretized) autonomous PDE. This leads to the *prediction* (forecast)

$$\widehat{\boldsymbol{z}}_{j+1} = \mathcal{P}(\boldsymbol{z}_j), \quad j = 1, \dots, J-1. \tag{1}$$

Here, and in what follows, $\widehat{(\cdot)}$ denotes a predicted quantity.

Let $\mathcal{H} : \mathbb{R}^{N_z} \to \mathbb{R}^{N_d}$ denote the observation operator, which maps the state to the observation space. If both the dynamical model (1), and the observation operator $\mathcal{H}$ are linear, and if model errors are Gaussian (or zero), along with Gaussian measurement errors with zero mean and known covariance, then the Kalman filter provides the optimal state estimate [57]. For nonlinear problems, the extended Kalman filter (EKF) [58] linearizes the dynamics and observation operator so that the Kalman filter can be applied locally. However, the cost of propagating the full state covariance matrix is prohibitive for high-dimensional (in state space) problems. To address this challenge, the EnKF [26] approximates the covariance using an ensemble of N_e states

$$Z_j = \left[\boldsymbol{z}_j^{(1)}, \cdots, \boldsymbol{z}_j^{(N_e)}\right], \quad j = 1, \dots, J, \tag{2}$$

where $Z_j \in \mathbb{R}^{N_z \times N_e}$. Similarly we introduce

$$\widehat{Z}_{j+1} = \left[\widehat{\boldsymbol{z}}_{j+1}^{(1)}, \cdots, \widehat{\boldsymbol{z}}_{j+1}^{(N_e)}\right], \quad j = 0, \dots, J-1, \tag{3}$$

$$\mathcal{H}\big(\widehat{Z}_{j+1}\big) = \left[\mathcal{H}\big(\widehat{\boldsymbol{z}}_{j+1}^{(1)}\big), \cdots, \mathcal{H}\big(\widehat{\boldsymbol{z}}_{j+1}^{(N_e)}\big)\right], \quad j = 0, \dots, J-1. \tag{4}$$

Using $\widehat{Z}_{j+1}$ and $\mathcal{H}\big(\widehat{Z}_{j+1}\big)$ the analysis operator for the EnKF may be defined and takes the form $\mathcal{A} : \mathbb{R}^{N_z \times N_e} \times \mathbb{R}^{N_d} \to \mathbb{R}^{N_z \times N_e}$. From it we obtain the analysis step

$$Z_{j+1} = \mathcal{A}(\widehat{Z}_{j+1}; \boldsymbol{d}_{j+1}), \quad j = 1, \dots, J-1, \tag{5}$$

which updates the ensemble of states to obtain Z_{j+1} from the predicted states $\widehat{Z}_{j+1}$ and the sensor data $\boldsymbol{d}_{j+1} \in \mathbb{R}^{N_d}$. The standard EnKF cycle can then be summarized as

$$Z_{j+1} = \mathcal{A}\big(\mathcal{P}(Z_j); \boldsymbol{d}_{j+1}\big), \quad j = 1, \dots, J-1, \tag{6}$$

where we apply the prediction operator columnwise to Z_j.

We next describe how to realize the analysis operator $\mathcal{A}$ in (5) using the EnKF. From the forecast ensemble $\widehat{Z}_{j+1}$ we compute the ensemble mean

$$\overline{\widehat{\boldsymbol{z}}}_{j+1} = \frac{1}{N_e} \sum_{n=1}^{N_e} \widehat{\boldsymbol{z}}_{j+1}^{(n)}, \tag{7}$$

and the ensemble perturbations

$$\widehat{Z}'_{j+1} = \frac{1}{\sqrt{N_e - 1}} \left[\widehat{\boldsymbol{z}}_{j+1}^{(1)} - \overline{\widehat{\boldsymbol{z}}}_{j+1}, \dots, \widehat{\boldsymbol{z}}_{j+1}^{(N_e)} - \overline{\widehat{\boldsymbol{z}}}_{j+1}\right]. \tag{8}$$

We also compute the predicted observations

$$\widehat{Y}_{j+1} = \left[\widehat{\boldsymbol{y}}_{j+1}^{(1)}, \ldots, \widehat{\boldsymbol{y}}_{j+1}^{(N_e)}\right] = \left[\mathcal{H}(\widehat{\boldsymbol{z}}_{j+1}^{(1)}), \ldots, \mathcal{H}(\widehat{\boldsymbol{z}}_{j+1}^{(N_e)})\right], \tag{9}$$

where

$$\boldsymbol{y}_j^{(n)} = \mathcal{H}(\boldsymbol{z}_j^{(n)}), \quad j = 1, \ldots, J, \tag{10}$$

so that $\widehat{Y}_{j+1} \in \mathbb{R}^{N_d \times N_e}$. From this we can define the predicted observation mean

$$\overline{\widehat{\boldsymbol{y}}}_{j+1} = \frac{1}{N_e} \sum_{n=1}^{N_e} \widehat{\boldsymbol{y}}_{j+1}^{(n)}, \tag{11}$$

and the associated perturbations

$$\widehat{Y}'_{j+1} = \frac{1}{\sqrt{N_e - 1}} \left[\widehat{\boldsymbol{y}}_{j+1}^{(1)} - \overline{\widehat{\boldsymbol{y}}}_{j+1} \quad \ldots \quad \widehat{\boldsymbol{y}}_{j+1}^{(N_e)} - \overline{\widehat{\boldsymbol{y}}}_{j+1}\right]. \tag{12}$$

Let $R \in \mathbb{R}^{N_d \times N_d}$ denote the observation-error covariance, and draw independent perturbations $\boldsymbol{\eta}_{j+1}^{(n)} \sim \mathcal{N}(0, R)$. Then the forecast states are updated based on the predicted observations and the observed data $\boldsymbol{d}_{j+1} \in \mathbb{R}^{N_d}$ as

$$\boldsymbol{z}_{j+1}^{(n)} = \widehat{\boldsymbol{z}}_{j+1}^{(n)} + \widehat{Z}'_{j+1} \widehat{Y}'^{T}_{j+1} \left(\widehat{Y}'_{j+1} \widehat{Y}'^{T}_{j+1} + R\right)^{-1} \left(\boldsymbol{d}_{j+1} + \boldsymbol{\eta}_{j+1}^{(n)} - \widehat{\boldsymbol{y}}_{j+1}^{(n)}\right). \tag{13}$$

Stacking into a matrix we obtain

$$Z_{j+1} = \left[\boldsymbol{z}_{j+1}^{(1)}, \cdots, \boldsymbol{z}_{j+1}^{(N_e)}\right], \quad j = 1, \ldots, J, \tag{14}$$

completing our definition of the analysis step $\widehat{Z}_{j+1} \mapsto Z_{j+1}$: here, (13) is a concrete realization of the analysis operator $\mathcal{A}$ in (5).

Remark 1. *Zhou et al. [3] explain the failure of the standard EnKF for problems with shocks in terms of pointwise violation of the unimodal (near Gaussian) behavior that is implicit in its derivation. An alternative perspective follows from function approximation. The EnKF subspace property [59], discussed for inverse problems in [60], implies that each analysis ensemble member* $z_{j+1}^{(m)}$ *lies in the linear span of the forecast ensemble* $\widehat{Z}_{j+1}$. *Consequently, applying the standard EnKF analysis step directly in physical state space leads to approximation of shock profiles in the linear span of other shock profiles. When shock locations differ across ensemble members, these linear combinations distort sharp features; such features are preserved only when they are aligned throughout the forecast ensemble.*

2.2. Transformed EnKF

The standard EnKF formulation in Subsection 2.1, and in particular the update formulae (13) together with Remark 1, make explicit that each analysis update lies in the linear span of the forecast ensemble. This linear span is generally not well suited to approximating functions with shocks and other discontinuities. The morphing EnKF [31, 33] and recent neural-network-based approaches [3, 30] both address this issue by applying the EnKF in a latent space. The morphing EnKF constructs a latent representation consisting of a registration map and aligned state representations, whereas the neural network-based methods employ learned latent representations. This observation motivates a general framework for applying the EnKF in feature-preserving latent spaces.

Let $\mathcal{T} : \mathbb{R}^{N_z} \to \mathbb{R}^{N_\phi}$ denote a transformation from physical state space to a latent space of dimension N_ϕ such that

$$\widehat{\boldsymbol{\phi}}_{j+1}^{(n)} = \mathcal{T}(\widehat{\boldsymbol{z}}_{j+1}^{(n)}), \tag{15}$$

with $\widehat{\boldsymbol{\phi}}_{j+1}^{(n)} \in \mathbb{R}^{N_\phi}$. Assume that it admits a reconstruction map $\mathcal{T}^{-1} : \mathbb{R}^{N_\phi} \to \mathbb{R}^{N_z}$ with small reconstruction error, $\|\mathcal{T}^{-1}(\mathcal{T}(\boldsymbol{z})) - \boldsymbol{z}\|_2^2$; $\mathcal{T}^{-1}$ is thus an approximate inverse. The corresponding latent space DA cycle is then

$$Z_{j+1} = \mathcal{T}^{-1}\Big(\mathcal{A}\big(\mathcal{T}\big(\mathcal{P}(Z_j)\big); \boldsymbol{d}_{j+1}\big)\Big), \quad j = 1, \ldots, J-1. \tag{16}$$

Here, $\mathcal{T}$ and $\mathcal{T}^{-1}$ are applied columnwise to the state ensemble. Thus, (16) is the latent space analogue of the standard EnKF cycle (6).

Next, define the ensemble

$$\widehat{\Phi}_{j+1} = \left[\widehat{\boldsymbol{\phi}}_{j+1}^{(1)}, \ldots, \widehat{\boldsymbol{\phi}}_{j+1}^{(N_e)}\right], \tag{17}$$

with mean

$$\overline{\widehat{\boldsymbol{\phi}}}_{j+1} = \frac{1}{N_e} \sum_{n=1}^{N_e} \widehat{\boldsymbol{\phi}}_{j+1}^{(n)}, \tag{18}$$

and perturbations

$$\widehat{\Phi}'_{j+1} = \frac{1}{\sqrt{N_e - 1}} \left[\widehat{\boldsymbol{\phi}}_{j+1}^{(1)} - \overline{\widehat{\boldsymbol{\phi}}}_{j+1} \quad \cdots \quad \widehat{\boldsymbol{\phi}}_{j+1}^{(N_e)} - \overline{\widehat{\boldsymbol{\phi}}}_{j+1}\right]. \tag{19}$$

Define $\mathcal{H}_\phi : \mathbb{R}^{N_\phi} \to \mathbb{R}^{N_d}$ by $\mathcal{H}_\phi = \mathcal{H} \circ \mathcal{T}^{-1}$. Then we can compute the predicted observations from the transformed state using

$$\widehat{\boldsymbol{y}}_{\phi,j+1}^{(n)} = \mathcal{H}_\phi(\widehat{\boldsymbol{\phi}}_{j+1}^{(n)}). \tag{20}$$

This yields the ensemble-predicted observations

$$\widehat{Y}_{\phi,j+1} = \left[\widehat{\boldsymbol{y}}_{\phi,j+1}^{(1)}, \ldots, \widehat{\boldsymbol{y}}_{\phi,j+1}^{(N_e)}\right] = \left[\mathcal{H}_\phi(\widehat{\boldsymbol{\phi}}_{j+1}^{(1)}), \ldots, \mathcal{H}_\phi(\widehat{\boldsymbol{\phi}}_{j+1}^{(N_e)})\right], \tag{21}$$

with mean

$$\overline{\widehat{\boldsymbol{y}}}_{\phi,j+1} = \frac{1}{N_e} \sum_{n=1}^{N_e} \widehat{\boldsymbol{y}}_{\phi,j+1}^{(n)}, \tag{22}$$

and perturbations

$$\widehat{Y}'_{\phi,j+1} = \frac{1}{\sqrt{N_e - 1}} \left[\widehat{\boldsymbol{y}}^{(1)}_{\phi,j+1} - \overline{\widehat{\boldsymbol{y}}}_{\phi,j+1} \quad \ldots \quad \widehat{\boldsymbol{y}}^{(N_e)}_{\phi,j+1} - \overline{\widehat{\boldsymbol{y}}}_{\phi,j+1} \right]. \tag{23}$$

Then the analysis update in the latent space can be written

$$\boldsymbol{\phi}^{(n)}_{j+1} = \widehat{\boldsymbol{\phi}}^{(n)}_{j+1} + \widehat{\Phi}'_{j+1} \widehat{Y}'^{T}_{\phi,j+1} \left(\widehat{Y}'_{\phi,j+1} \widehat{Y}'^{T}_{\phi,j+1} + R \right)^{-1} \left(\boldsymbol{d}_{j+1} + \boldsymbol{\eta}^{(n)}_{j+1} - \widehat{\boldsymbol{y}}^{(n)}_{\phi,j+1} \right). \tag{24}$$

We may stack these as in (14) to obtain Φ_{j+1}, completing our definition of the analysis step $\widehat{\Phi}_{j+1} \mapsto \Phi_{j+1}$. We then recover the analysis state in the original state space as $Z_{j+1} = \mathcal{T}^{-1}(\Phi_{j+1})$, thus completing our definition of the transformed analysis step $\widehat{Z}_{j+1} \overset{\mathcal{T}}{\mapsto} Z_{j+1}$. Note that the sensor data $\boldsymbol{d}_{j+1}$ and observation-error covariance R remain defined in the original observation space.

2.3. Constructing Latent Space Transformations

As outlined in Subsection 1.4, we seek a transformation $\mathcal{T}$ with small reconstruction error, a feature-preserving reconstruction map $\mathcal{T}^{-1}$, and a latent representation that varies smoothly across ensemble members. The morphing EnKF [31, 33] achieves these properties through image registration: the latent variables comprise aligned state representations and registration maps, which vary smoothly across the ensemble, while the inverse transformation reconstructs sharp features by warping the aligned state with the registration map. The neural-network-based approaches [3, 30] instead learn the latent transformation from data. Both neural-network-based approaches include a reconstruction loss, while nonlinear activation functions promote feature-preserving reconstructions. In addition, the neural EnKF [3] encourages latent-space smoothness through nearest-neighbor chain training, whereas the decoder-based approach [30] promotes it implicitly through the joint learning of latent variables and a shared decoder.

In the morphing EnKF, the reconstruction map $\mathcal{T}^{-1}$ is obtained by applying the inverse registration map to the aligned state representation, whereas in the neural-network-based approaches it is specified by the neural network architecture. In both cases, the corresponding encoding map $\mathcal{T}$ is defined implicitly, either by solving a registration problem or through neural network training. Following this perspective, throughout this paper, we specify $\mathcal{T}^{-1}$ explicitly and define $\mathcal{T}$ implicitly through an optimization problem.

2.4. Transformed EnKF for a Hyperbolic Tangent Profile

Consider the parameterized hyperbolic tangent

$$H_\delta(x; c_L, c_R, x_s) = \frac{c_L + c_R}{2} - \frac{c_L - c_R}{2} \tanh\left(\frac{x - x_s}{\delta} \right). \tag{25}$$

We define the reconstruction $\mathcal{T}^{-1} : \mathbb{R}^{N_\phi} \to C(\Omega)$ by

$$\mathcal{T}^{-1}(\boldsymbol{\phi})(x) = H_\delta(x; c_L, c_R, x_s), \tag{26a}$$

with transformed coordinates

$$\boldsymbol{\phi} = (c_L, c_R, x_s, \delta) \in \mathcal{X} \tag{26b}$$

and latent space

$$\mathcal{X} \equiv \mathbb{R} \times \mathbb{R} \times \Omega \times \mathbb{R}_{>0}. \tag{26c}$$

We then define $\mathcal{T} : C(\Omega) \to \mathbb{R}^{N_\phi}$ through the minimization problem

$$\boldsymbol{\phi}_* = \arg\min_{\boldsymbol{\phi} \in \mathcal{X}} J(\boldsymbol{\phi}; c_L, c_R, x_s, \delta), \tag{27a}$$

with objective function

$$J(\boldsymbol{\phi}; c_L, c_R, x_s, \delta) = \int_\Omega \left| \mathcal{T}^{-1}(\boldsymbol{\phi})(x) - H_\delta(x; c_L, c_R, x_s) \right|^2 dx. \tag{27b}$$

so that

$$\mathcal{T}\big(H_\delta(x; c_L, c_R, x_s)\big) = (c_L, c_R, x_s, \delta). \tag{27c}$$

No regularization is needed to promote latent space smoothness because, in this special case, the reconstruction map exactly matches the parameterization used to generate the data, whose latent variables are Gaussian.

We now demonstrate the transformed EnKF for (25) with reconstruction function (26). We set $\Omega \equiv [0, 1]$ with grid $x_i = i\Delta x$ for $i = 0, \ldots, N_z - 1$, where $\Delta x = 1/(N_z - 1)$, so that $\boldsymbol{x} \in \mathbb{R}^{N_z}$. In the numerical experiments presented below we take $N_z = 400$ and $\delta = 4\Delta x$, with the same width for both the reference truth and all ensemble members. We define a reference truth profile $\boldsymbol{z}^\dagger = H_\delta(\boldsymbol{x}; c_L^\dagger, c_R^\dagger, x_s^\dagger)$, with $c_L^\dagger = 2$, $c_R^\dagger = 1$, and $x_s^\dagger = 0.55$, which we will observe noisily at four points evenly distributed between $x = 0.2$ and $x = 0.8$. Let $\boldsymbol{x}_{\text{obs}} \in \mathbb{R}^{N_d}$ denote these points, with

$$x_{\text{obs},i} = 0.2 + i0.2, \quad i = 0, \ldots, 3. \tag{28}$$

The corresponding data vector $\boldsymbol{d} \in \mathbb{R}^{N_d}$ has entries

$$d_i = H_\delta(x_{\text{obs},i}, c_L^\dagger, c_R^\dagger, x_s^\dagger) + \eta_i, \quad i = 0, \ldots, N_d - 1, \tag{29}$$

where $\boldsymbol{\eta} \sim \mathcal{N}(0, R)$ for the observation-error covariance R, whose diagonal entries are given by $R_{ii} = \max\{0.1 d_i, 0.05\}$. This choice imposes a relative observation error of 10% and an absolute error of 0.05.

Remark 2. *In Subsection 2.1, we introduce the state vector $\boldsymbol{z}_{j+1} \in \mathbb{R}^{N_z}$. For one-dimensional problems, N_z is equal to the number of grid points in the x direction. We use the notation N_z instead of N_x for consistency with Subsection 2.1.*

We construct an ensemble of $N_e = 30$ members by sampling, for $n = 1, \ldots, N_e$,

$$c_L^{(n)} \sim \mathcal{N}(2, 0.2^2), \quad c_R^{(n)} \sim \mathcal{N}(1, 0.1^2), \quad x_s^{(n)} \sim \mathcal{N}(0.5, 0.05^2), \tag{30}$$

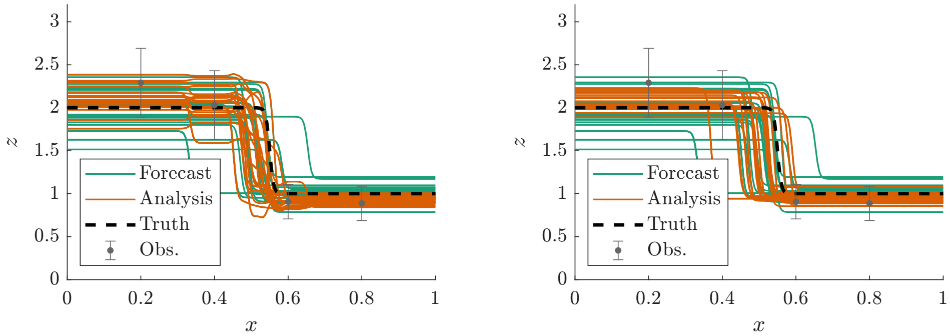

(a) Standard EnKF

(b) Transformed EnKF

Figure 1: Forecast and analysis ensembles for the parameterized hyperbolic tangent profile (25). The transformed EnKF is feature-preserving, while the standard EnKF introduces spurious oscillations.

and setting $\boldsymbol{z}^{(n)} = H_\delta(\boldsymbol{x}; c_L^{(n)}, c_R^{(n)}, x_s^{(n)})$. Thus, the ensemble-mean shock location,

$$\overline{x}_s = \frac{1}{N_e} \sum_{n=1}^{N_e} x_s^{(n)} = 0.5,$$

differs from the reference truth value $x_s^\dagger = 0.55$.

Figure 1a shows that, although the forecast ensemble consists entirely of hyperbolic tangent profiles, the analysis ensemble produced by the standard EnKF (13) does not. The linear EnKF update in the physical state space introduces spurious oscillations near the discontinuity (see Remark 1). In contrast, Figure 1b shows that performing the analysis step with the transformed EnKF (24) in the latent variables defined by (27) preserves the hyperbolic tangent structure. This is because the reconstruction map (26) enforces hyperbolic tangent profiles by construction.

3. Level Set Representations for 1D Scalar Fields

In this section, we generalize the transformed EnKF approach of Subsection 2.4 by allowing the left and right states to vary with x, rather than remain constant, to better represent the spatially varying functions encountered in compressible flows. We formulate a regularized optimization problem to identify the level set representation, such that uncertainty in the shock location is decoupled from uncertainty in the solution on either side of the shock. This decoupling yields a representation that varies smoothly across ensembles of similar solutions, and hence identifies a latent space that is favorable for the analysis step in the DA cycle. In Subsection 3.1, we consider problems with a single discontinuity and define a regularized optimization problem that ensures the desired properties of the level set representation. In Subsection 3.2 we extend the methodology to multiple discontinuities. The key ideas, namely the level set representation and the optimization problem to determine it, are contained in the main body of the text; details of our specific implementation of the methodology are presented in Appendix C.

3.1. 1D Level Set Representation for a Scalar Field with a Single Discontinuity

For a single discontinuity in 1D, we propose the reconstruction map

$$\mathcal{T}^{-1}(\boldsymbol{\phi})(x) = \frac{f_L(x) + f_R(x)}{2} - \frac{f_L(x) - f_R(x)}{2} \tanh\left(\frac{x - x_s}{\delta}\right), \tag{31a}$$

where

$$\boldsymbol{\phi} = (f_L, f_R, x_s, \delta), \qquad \boldsymbol{\phi} \in \mathcal{X} \tag{31b}$$

for

$$\mathcal{X} \equiv C^1(\Omega) \times C^1(\Omega) \times \Omega \times \mathbb{R}_{>0}. \tag{31c}$$

Here, $C^1(\Omega)$ is the space of functions on Ω with continuous first derivatives, f_L and f_R are smooth, globally defined, state extensions to the left and right of the discontinuity, respectively, x_s is an estimate of the discontinuity location, and δ is an estimate of its width.

Remark 3. *As discussed in Subsection 1.4, we seek a feature-preserving latent representation, so that perturbations in latent variables preserve sharp features in physical space. In the present setting, this property is achieved through the nonlinear reconstruction map* (31a)*, which introduces nonlinearity through the hyperbolic tangent function. Similarly, neural network-based approaches obtain nonlinear reconstruction maps through their activation functions, while the morphing EnKF does so through its registration map. This nonlinearity is important because the standard EnKF analysis update is confined to the linear span of the forecast ensemble; as discussed in Remark 1, linear combinations of states with misaligned discontinuities generally do not preserve sharp features. Thus, for ensembles with uncertain discontinuity locations, feature-preserving latent representations generally require a nonlinear reconstruction map.*

Remark 4. *We refer to* (31a) *as a level set representation because the discontinuity is encoded by the location x_s, which is the zero level set of the signed distance function*

$$\varphi(x) = x - x_s. \tag{32}$$

We do not explicitly use this level set function in 1D, since the discontinuity location can be parameterized directly by x_s. In 2D, however, the discontinuity is a curve, so we parameterize it by a level set function rather than by a sequence of points; see Section 5.

3.1.1. Regularized Optimization Problem For The Level Set Representation

We seek x_s, f_L, and f_R such that the reconstruction map (31) accurately approximates the function f while the associated level set representations vary smoothly across an ensemble of similar functions. In particular, we seek to encode all information about the shock location in x_s, rather than in f_L and f_R. To achieve this, we solve the regularized minimization problem

$$\boldsymbol{\phi}_* = \underset{\boldsymbol{\phi} \in \mathcal{X}}{\arg\min}\, J(\boldsymbol{\phi}; f), \tag{33a}$$

with objective function

$$
\begin{aligned}
J(\boldsymbol{\phi}) = &\int_\Omega \left|\mathcal{T}^{-1}(\boldsymbol{\phi})(x) - f(x)\right|^2 dx \\
&+ \lambda_1 \int_\Omega \left(|f_L'(x)|^2 + |f_R'(x)|^2\right) dx \\
&+ \lambda_b(|f_L(a) - f(a)|^2 + |f_R(b) - f(b)|^2).
\end{aligned}
\tag{33b}
$$

Here, λ_1 and λ_b are regularization parameters, where λ_1 promotes smoothness while λ_b enforces boundary conditions.

We solve (33) using a bound-constrained trust-region reflective nonlinear least-squares method, with the Jacobian approximated using two-point finite differences. However, directly solving this problem from an arbitrary initialization can converge slowly. We therefore introduce several modifications to reduce computational cost and improve convergence, as detailed in Appendix C. We briefly summarize the main ideas here.

Although (33) is formulated globally in x, we show in Appendix C.2 how to formulate a local optimization problem over a neighborhood of the discontinuity. This reduces the number of unknowns and residuals, yielding a smaller Jacobian and decreasing the computational cost. We first estimate x_s using the gradient of f and identify a neighborhood about x_s bounded by local minima of the gradient magnitude. We also construct smooth initial guesses for f_L and f_R that yield a small reconstruction error. These choices provide an informed initialization, and the optimization then refines the representation within this neighborhood. We impose the bounds $\delta \in [0.1\Delta x, 100\Delta x]$ and $x_s \in \Omega$, while leaving f_L and f_R unbounded.

Remark 5. *Note that, without regularization, one can obtain zero reconstruction error by taking $f_L(x) = f(x)$ and $f_R(x) = f(x)$, with any $\delta > 0$ and $x_s \in \Omega$. However, such a solution encodes the shock location in f_L and f_R, rather than solely in x_s. Consequently, f_L and f_R will not vary smoothly across an ensemble of similar functions, and the resulting level set representation fails to satisfy the desired criteria.*

Remark 6. *The parameters λ_1 and λ_b balance reconstruction accuracy, smoothness of the state extensions, and agreement with the boundary values. As discussed in Remark 5, insufficient regularization allows the state extensions to encode information about the shock location, which we wish to avoid. In contrast, excessively large values of λ_1 yield smooth but inaccurate state extensions. We therefore seek the smallest λ_1 that suppresses shock-like gradients in f_L and f_R while yielding accurate reconstruction. The parameter λ_b controls agreement with the boundary values, which are imposed through a penalty rather than as hard constraints. It can be increased until the boundary mismatch falls below a user-prescribed tolerance. The regularization parameters are problem specific and should be tuned on representative ensemble members, assessing both reconstruction accuracy and smoothness of the state extensions across ensemble members. Representative values for 1D compressible flows are presented in Table 1 of Subsection 4.1.*

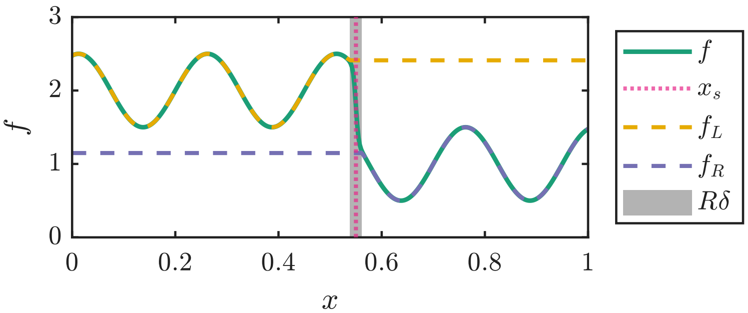

Figure 2: Identifying the level set representation of (34) by solving (33). Implementation details are presented in Appendix C. We visualize the width by shading $x \in [x_s - R\delta/2, x_s + R\delta/2]$.

Remark 7. *For simplicity, we approximate the entire Jacobian using finite differences. Localizing the optimization problem substantially reduces the cost of this approximation. Further efficiencies could be achieved by exploiting the structure of the level set representation. In particular, the derivative of the hyperbolic tangent is available analytically, while the Jacobians of the smooth functions on either side of the discontinuity could be computed using automatic differentiation. Alternatively, the smooth functions could be represented using a low-dimensional basis, resulting in lower-dimensional Jacobians that can be evaluated analytically.*

3.1.2. Demonstration of the The Level Set Representation

Here, we demonstrate the level set representation (31a) for

$$f(x) = \frac{3}{2} + \frac{1}{2}\sin(8\pi(x - 0.2)) - \frac{1}{2}\tanh\left(\frac{x - x_s^\dagger}{\delta^\dagger}\right) \tag{34}$$

defined over $\Omega \equiv [0, 1]$, with discontinuity location $x_s^\dagger = 0.5$, and width $\delta^\dagger = 0.02$. Figure 2 depicts (34) along with its level set representation, showing f_L, f_R, and x_s. We visualize the width by shading the region between the two points where $\tanh((x - x_s)/\delta)$ achieves 1% and 99% of its maximum value, denoted. This region has width $R\delta$, for $R \approx 4.60$, and the corresponding interval is $[x_s - R\delta/2, x_s + R\delta/2]$. Figure 2 highlights an advantage of the level set EnKF: its latent representation is physically interpretable. The resulting interpretability facilitates understanding the action of the filter and enables the incorporation of problem-specific inductive biases.

3.2. 1D Level Set Representation for a Scalar Field with Multiple Discontinuities

This subsection modifies the 1D level set procedure presented in Subsection 3.1 so that it can be applied to a scalar field $f(x)$ with multiple discontinuities. Throughout this subsection, we will assume that the number of discontinuities, K, is known *a priori*.

For K discontinuities in one space dimension, our reconstruction map becomes

$$\mathcal{T}^{-1}(\boldsymbol{\phi})(x) = \sum_{k=0}^{K} \alpha_k(x) f_k(x), \tag{35a}$$

where

$$\alpha_0(x) = \prod_{j=1}^{K} \left(1 - H_j(x)\right),$$
$$\alpha_k(x) = \left(\prod_{j=1}^{k} H_j(x)\right)\left(\prod_{j=k+1}^{K} \left(1 - H_j(x)\right)\right), \quad k = 1, \ldots, K-1, \tag{35b}$$
$$\alpha_K(x) = \prod_{j=1}^{K} H_j(x),$$

for

$$H_j(x) = \frac{1}{2}\left[1 + \tanh\left(\frac{x - x_{s,j}}{\delta_j}\right)\right], \quad j = 1, \ldots, K. \tag{35c}$$

The latent variables are then

$$\boldsymbol{\phi} = \left(f_0, \ldots, f_K, x_{s,1}, \ldots, x_{s,K}, \delta_1, \ldots, \delta_K\right), \tag{35d}$$

where

$$\boldsymbol{\phi} \in \mathcal{X}_K, \quad \mathcal{X}_K \equiv \left(C^1(\Omega)\right)^{K+1} \times \Omega_<^K \times \mathbb{R}_{>0}^K, \tag{35e}$$

with

$$\Omega_<^K = \{(x_{s,1}, \ldots, x_{s,K}) \in \Omega^K : x_{s,1} < \cdots < x_{s,K}\}. \tag{35f}$$

In principle, we wish to solve the regularized minimization problem

$$\boldsymbol{\phi}_* = \underset{\boldsymbol{\phi} \in \mathcal{X}_K}{\arg\min}\, J(\boldsymbol{\phi}; f), \tag{36a}$$

with objective function

$$\begin{aligned} J(\boldsymbol{\phi}) = &\int_\Omega \left|\mathcal{T}^{-1}(\boldsymbol{\phi})(x) - f(x)\right|^2 dx \\ &+ \lambda_1 \sum_{k=0}^{K} \int_\Omega \left(|f_k'(x)|^2\right) dx \\ &+ \lambda_b(|f_0(a) - f(a)|^2 + |f_K(b) - f(b)|^2). \end{aligned} \tag{36b}$$

Although we could attempt to directly solve (36) using a nonlinear least-squares solver, it is more effective to reformulate it as multiple local optimization problems. To do so, we first estimate the centers of the K discontinuities using the local maxima of the gradient of f. We then define a neighborhood around each discontinuity, bounded by local minima of the gradient of f. This decomposition allows us to solve K local regularized minimization problems independently. As in the case of a single discontinuity described in Subsubsection 3.1.1, the optimization need only determine a small local correction to $\boldsymbol{\phi}$ near each of the K discontinuities, rather than optimize from an arbitrary initial guess globally in x. We provide a detailed description of this procedure in Appendix C.4.

4. Level Set EnKF for 1D Compressible Flows

This section is concerned with applying the level set EnKF to 1D compressible Euler problems. Subsection 4.1 describes the demonstration problems, Subsection 4.2 describes the setup of our filtering problem and how we evaluate EnKF performance. Subsection 4.3 extends the level set representation procedure of Section 3 to solutions to the 1D compressible Euler equations, while Subsection 4.4 describes how to construct level set representations for an ensemble of flow states, and then how to apply the EnKF analysis step (24) to the resulting level set representations. Finally, Subsection 4.5 demonstrates the level set EnKF for the problems outlined in Subsection 4.1.

4.1. Description of Demonstration Problems

We apply the level set EnKF to three solutions of the 1D compressible Euler equations: Toro's shock tube problem [36], the Shu-Osher shock-entropy problem [55], and Sod's shock tube problem [56]. These problems were previously studied by Subrahmanya and Sandu [27] in their development of the ETPF-DTW approach. We use the same problems because, together, they contain the canonical flow features present in compressible flows: shocks, contact surfaces, and rarefaction waves.

The initial conditions for our demonstration problems take the form

$$\boldsymbol{w}(x) = \begin{cases} \boldsymbol{w}_L(x), & x \leq x_d, \\ \boldsymbol{w}_R(x), & x > x_d, \end{cases}, \quad x \in \Omega. \tag{37}$$

for $\Omega \equiv [0,1]$. Here, $\boldsymbol{w} = (\rho, u, p)$ denotes the vector of primitive variables and x_d denotes the location of a diaphragm separating the left state $\boldsymbol{w}_L(x)$ from the right state $\boldsymbol{w}_R(x)$. Thus, the initial condition $\boldsymbol{w}(x)$ is discontinuous at $x = x_d$. At time $t = 0$, the diaphragm is removed, allowing the two states to interact.

We discretize the spatial domain Ω uniformly using N_x grid points:

$$x_i = i\Delta x, \qquad i = 0, \ldots, N_x - 1, \qquad \Delta x = \frac{1}{N_x - 1}. \tag{38}$$

The resulting vector of grid-point coordinates is $\boldsymbol{x} \in \mathbb{R}^{N_x}$. We specify problem-specific final times, T, and choose time steps satisfying the CFL condition. For each calculation, the values of N_x and T are listed in Table 1.

Subsubsections 4.1.1, 4.1.2, and 4.1.3, describe the initial conditions and resulting solutions for Toro's shock tube problem, the Shu-Osher shock-entropy problem, and Sod's shock tube problem, respectively. The variables used to define the initial conditions are presented in Table 2.

4.1.1. Toro's Shock Tube Problem

Toro [36] introduces a shock tube problem with initial left and right states that are spatially constant. The resulting solution comprises two shocks and a contact surface, all traveling to the right.

	T	$t_{\mathrm{DA},1}$	Δt_{DA}	N_x	λ_1	λ_b
Toro	0.399	0.007	0.0035	400	10^2	10^2
Shu-Osher	0.25	0.025	0.0125	800	10^{-1}	10^2
Sod	0.2	0.06	0.01	400	10^2	10^2

Table 1: Final time T, time of first DA cycle $t_{\mathrm{DA},1}$, spacing of subsequent DA cycles Δt_{DA}, spatial resolution N_x, and level set regularization parameters λ_1 and λ_b for the 1D Euler experiments.

4.1.2. Shu-Osher Shock-Entropy Problem

The solution to Toro's shock tube problem is nearly piecewise constant, so we apply our method to the Shu-Osher shock-entropy problem [55] to highlight that it can be applied to more complicated functions. All fields of the initial left and right states are spatially constant except for the density field to the right of the diaphragm, which varies sinusoidally as

$$\rho_R(x) = \widetilde{\rho}_R + 0.2\sin\left(10\pi(x - x_d)\right). \tag{39}$$

The solution comprises a right-going shock interacting with an entropy wave.

4.1.3. Sod's Shock Tube Problem

Sod's shock tube problem [56] serves as our final demonstration problem. All fields of the initial left and right states are spatially constant, and the solution comprises a left-going rarefaction wave, a right-going contact surface, and a right-going shock.

4.2. Numerical Setup and Performance Metrics

Subsubsection 4.2.1 describes the filtering problem and observation setting for the 1D Euler experiments, while Subsubsection 4.2.2 describes the performance metrics used to assess level set EnKF.

4.2.1. Filtering Problem and Observation Setting

Uncertainty in the initial condition leads to uncertainty in our state estimate, which we reduce by solving the filtering problem using the transformed EnKF (24), with the level set representation as our latent variables. We assume that the parameters specifying the true initial condition (37) are known to problem-specific tolerances. Let X denote an uncertain parameter. For each such parameter, we draw each ensemble member independently according to

$$X^{(n)} \sim \mathcal{N}(\mu_X, \sigma_X^2), \quad n = 1, \ldots, N_e, \tag{40}$$

where μ_X and σ_X denote the mean and standard deviation, respectively. Table 2 reports these values along with the reference truth. Note that the ensemble means match the truth values for the left and right states, while the diaphragm-location means are intentionally offset from the truth to increase the uncertainty in the discontinuity locations.

We place pressure sensors at

$$x_{\mathrm{obs},i} = 0.2 + i0.2, \quad i = 0, \ldots, 3, \tag{41}$$

Problem	Statistic	ρ_L	u_L	p_L	ρ_R	u_R	p_R	x_d
Toro	Truth	5.99924	19.5975	460.894	5.99242	−6.19633	46.0950	0.41
	μ	$\rho_L^\dagger$	$u_L^\dagger$	$p_L^\dagger$	$\rho_R^\dagger$	$u_R^\dagger$	$p_R^\dagger$	0.5
	σ	0.2	0.0	46.0894	0.1	0.0	4.6095	0.1
Shu-Osher	Truth	3.857143	2.629369	10.33333	1.0	0.0	1.0	0.05
	μ	$\rho_L^\dagger$	$u_L^\dagger$	$p_L^\dagger$	$\rho_R^\dagger$	$u_R^\dagger$	$p_R^\dagger$	0.1
	σ	0.4	0.2	1.03333	0.1	0.0	0.1	0.04
Sod	Truth	1.0	0.0	1.0	0.125	0.0	0.1	0.59
	μ	$\rho_L^\dagger$	$u_L^\dagger$	$p_L^\dagger$	$\rho_R^\dagger$	$u_R^\dagger$	$p_R^\dagger$	0.5
	σ	0.05	0.0	0.05	0.006	0.0	0.005	0.1

Table 2: Truth parameters, as well as the means and standard deviations used to construct the initial ensembles for the 1D Euler experiments. For the Shu-Osher shock-entropy problem, ρ_R denotes $\tilde{\rho}_R^\dagger$ in (39).

so that $N_d = 4$. The data vector $\boldsymbol{d} \in \mathbb{R}^{N_d}$ has entries

$$d_i = p^\dagger(x_{\text{obs},i}, t; \boldsymbol{w}_L^\dagger, \boldsymbol{w}_R^\dagger, x_d^\dagger) + \eta_i, \quad i = 0, \dots, N_d - 1, \tag{42}$$

where $\boldsymbol{\eta} \sim \mathcal{N}(0, R)$ and $R_{ii} = \max\{0.1p^\dagger(x_{\text{obs},i}, t; \boldsymbol{w}_L^\dagger, \boldsymbol{w}_R^\dagger, x_d^\dagger), 0.05\}$, corresponding to 10% relative observation error with a minimum absolute error of 0.05. The reference pressure field $p^\dagger$ is obtained by solving the Euler equations numerically on a grid of size $N_x^\dagger = 4000$ and interpolating the solution to the observation point $x_{\text{obs},i}$.

We solve the filtering problem using ensembles of size $N_e = 50$, with the DA schedules listed in Table 1, where $t_{\text{DA},1}$ denotes the time of the first DA cycle and Δt_{DA} denotes the spacing between subsequent DA cycles. Table 1 also lists the regularization parameters λ_1 and λ_b used in (33) to construct the level set representation.

4.2.2. Performance Metrics

For an arbitrary field $\boldsymbol{f}_j \in \mathbb{R}^{N_x}$ at time index j, we compute the root mean square error (RMSE)

$$\text{RMSE}(\boldsymbol{f}_j) = \frac{1}{\sqrt{N_x}} \|\overline{\boldsymbol{f}}_j - \boldsymbol{f}_j^\dagger\|_2, \tag{43}$$

which measures the error between the ensemble mean and reference truth, while we compute the ensemble spread as

$$\text{Spread}(\boldsymbol{f}_j) = \sqrt{\frac{1}{N_x}\text{trace}(P(\boldsymbol{f}_j))}, \quad P(\boldsymbol{f}_j) = \frac{1}{N_e - 1}\sum_{n=1}^{N_e}(\boldsymbol{f}_j^{(n)} - \overline{\boldsymbol{f}}_j)(\boldsymbol{f}_j^{(n)} - \overline{\boldsymbol{f}}_j)^T, \tag{44}$$

which measures the uncertainty represented by the ensemble. The EnKF approximates the uncertainty in the state estimate using the sample covariance of an ensemble. If the EnKF is well calibrated, then the ensemble spread should provide a reasonable estimate of the actual estimation error. Consequently, the ensemble spread and the RMSE should be of

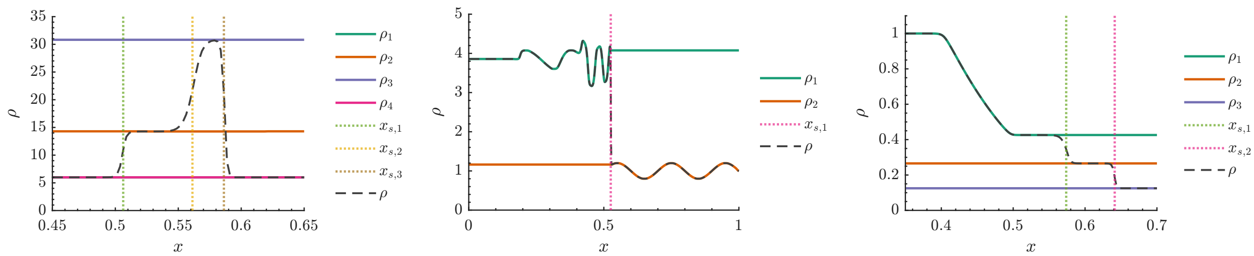

(a) Toro, $t = 0.007$. (b) Shu–Osher, $t = 0.12$. (c) Sod, $t = 0.08$.

Figure 3: Level set representations of the density fields for the one-dimensional Euler test problems: (a) Toro's shock tube problem, (b) the Shu-Osher shock-entropy problem, and (c) Sod's shock tube problem. The line for the ρ_1 component in Toro's shock tube problem is hidden by ρ_4, as they have the same value.

similar magnitude, and we assess performance by plotting both RMSE and ensemble spread as functions of DA cycle. We additionally define the *farthest ensemble member* to be the member with the largest Euclidean distance from the ensemble mean.

4.3. Level Set Representations for 1D Compressible Flows

For compressible flows, we apply the level set representation developed in Section 3 field-by-field to the primitive variables $\boldsymbol{w}$, computing the representation for each field independently. The resulting latent space representation for field $\boldsymbol{w}_i \in \mathbb{R}^{N_x}$ with K_i discontinuities is

$$\boldsymbol{\phi}_i = \begin{bmatrix} \boldsymbol{w}_{i,1} & \dots & \boldsymbol{w}_{i,K_i+1} & \boldsymbol{\varphi}_{i,1} & \dots & \boldsymbol{\varphi}_{i,K_i} & \delta_{i,1} & \dots & \delta_{i,K} \end{bmatrix}^T, \tag{45a}$$

where $\boldsymbol{w}_{i,k} \in \mathbb{R}^{N_x}$ for $k = 1, \dots, K_i + 1$, $\boldsymbol{\varphi}_{i,k} \in \mathbb{R}^{N_x}$ for $k = 1, \dots, K_i$, and $\delta_{i,k} \in \mathbb{R}_{>0}$ for $k = 1, \dots, K_i$. We then concatenate $\boldsymbol{\phi}_i \in \mathbb{R}^{(2K_i+1)\times N_x + K_i}$ for $i = 1, 2, 3$ to obtain

$$\boldsymbol{\phi} = \begin{bmatrix} \boldsymbol{\phi}_1 & \boldsymbol{\phi}_2 & \boldsymbol{\phi}_3 \end{bmatrix}^T, \tag{45b}$$

the level set representation of $\boldsymbol{w}$. Implementation details are presented in Appendix C.5.

Figure 3 plots the level set representation of the density field for each of the demonstration problems described in Subsection 4.1. We choose to plot the density field because it varies across the contact surface, while the velocity and pressure fields are constant. For ease of plotting, we plot the discontinuity location, rather than its level set function.

Remark 8. *As discussed in Subsubsection 1.2.3 and Appendix B, compressible flow solvers impose an intrinsic shock width, and preserving this width helps prevent spurious oscillations. Although we cannot sharpen shocks, contact surfaces can optionally be sharpened after fitting: we assign them the smallest fitted shock width in the corresponding flow field. This produces sharper contacts while retaining a width resolved by the numerical solver. In our experiments, this choice did not introduce spurious oscillations. This behavior is consistent with the findings of Fukushima and Kitamura [53].*

4.4. Level Set EnKF Formulation for Compressible Flows

As discussed in Remark 8, we wish for our level set representations to preserve the intrinsic shock width imposed by the compressible flow solver. Therefore, we wish treat shock and contact widths as a property of the discretization rather than as a state variable. Thus, we fit level set representations to each ensemble member such that they share the same shock and contact widths. To achieve this, we first fit level set representations to each ensemble member separately, and then use the median shock width (across ensemble members) as the shared event width. We then refit the level set representations using this shared prescribed shock width. Details are presented in Appendix C.5.

In addition, if a rarefaction wave is present, we align the corresponding state extensions using the procedure outlined in Appendix C.6, and augment the latent variables (45) with the affine-transformation parameters from (C.12). Finally, we apply the EnKF analysis step (24) to the level set representations, and then transform back to state space.

Remark 9. *The initial level set fits for different ensemble members can be computed in parallel. After computing the ensemble-median width for each primitive field, the refits can likewise be performed in parallel. This structure improves the scalability of the level set fitting step with increasing ensemble size.*

Remark 10. *To reduce computational cost, we could instead infer a shock width from a single ensemble member. However, this could result in a shock width that is not representative of the entire ensemble. Thus, we use the median of the ensemble of widths.*

Remark 11. *The alignment procedure for the rarefaction wave borrows ideas from image registration [32], which seeks to align different data sets onto a shared coordinate system. Image registration also underlies the morphing EnKF [31].*

4.5. Results

We now demonstrate the level set EnKF for 1D compressible flows. We show that our method preserves sharp features, while reducing RMSE. In addition, the ensemble spread is similar in magnitude to the RMSE, demonstrating that our ensemble accurately represents the uncertainty in our state. Subsubsections 4.5.1, 4.5.2, and 4.5.3 demonstrate the methodology for Toro' shock tube problem, the Shu-Osher shock-entropy problem, and Sod's shock tube problem, respectively.

4.5.1. Toro's Shock Tube Problem

Figure 4 plots the ensemble members against the reference truth for the initial condition and several representative analysis steps. Each analysis step preserves sharp features, while the ensemble converges to the reference truth as the number of DA cycles increases. Figure 5 shows that the RMSE converges and that the ensemble spread remains comparable in magnitude. The x-t diagrams in Figure 6 show that the largest correction occurs when, for a given member, the right shock reaches the rightmost pressure sensor. The subsequent update shifts the solution to the left, bringing it to closer agreement with the reference truth.

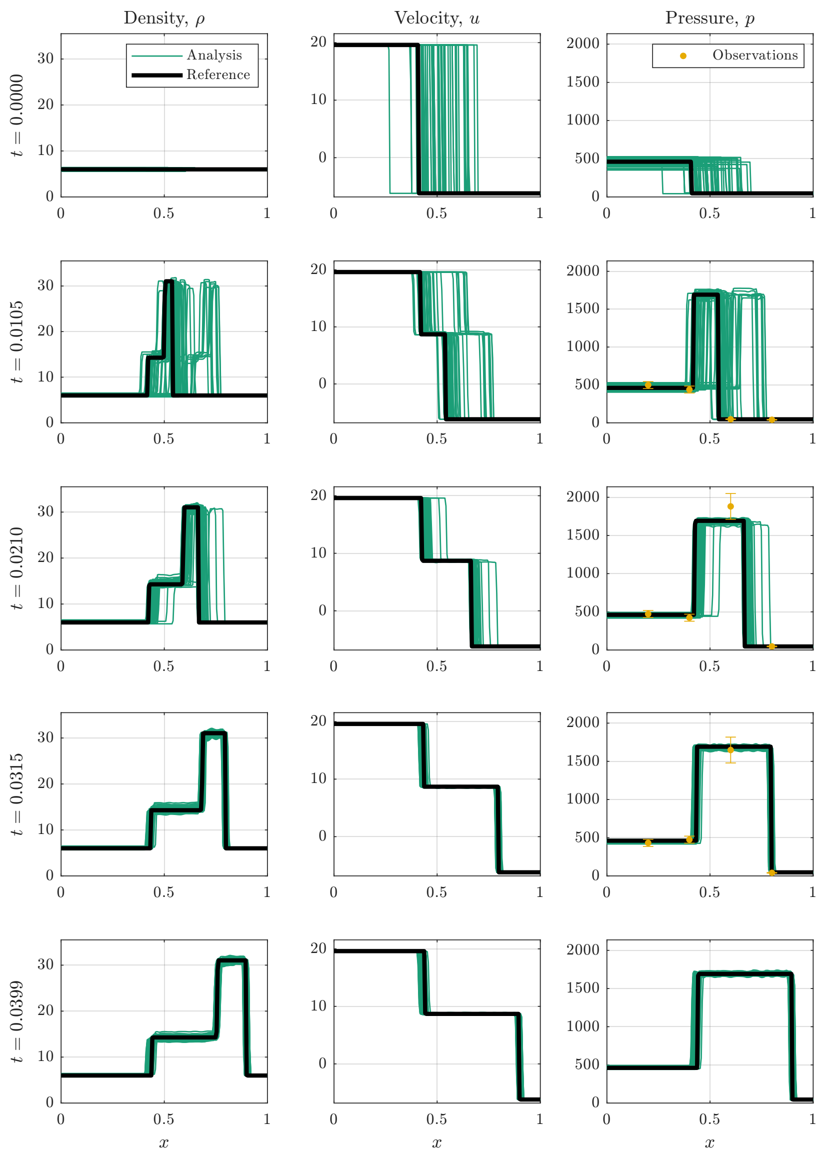

Figure 4: Analysis ensemble for Toro's shock tube problem, plotting the ensemble members against the reference truth immediately following the analysis step, for a subset of DA cycles. With increasing time, the ensemble members show better agreement with the reference truth.

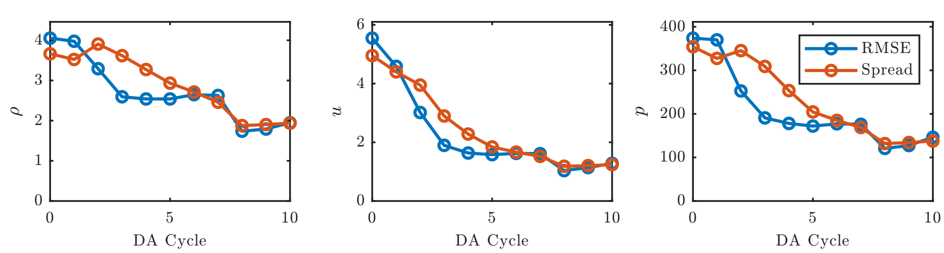

Figure 5: RMSE and spread as a function of DA cycle for Toro's shock tube problem. The values at DA cycle 0 correspond to the forecast value before the first DA cycle.

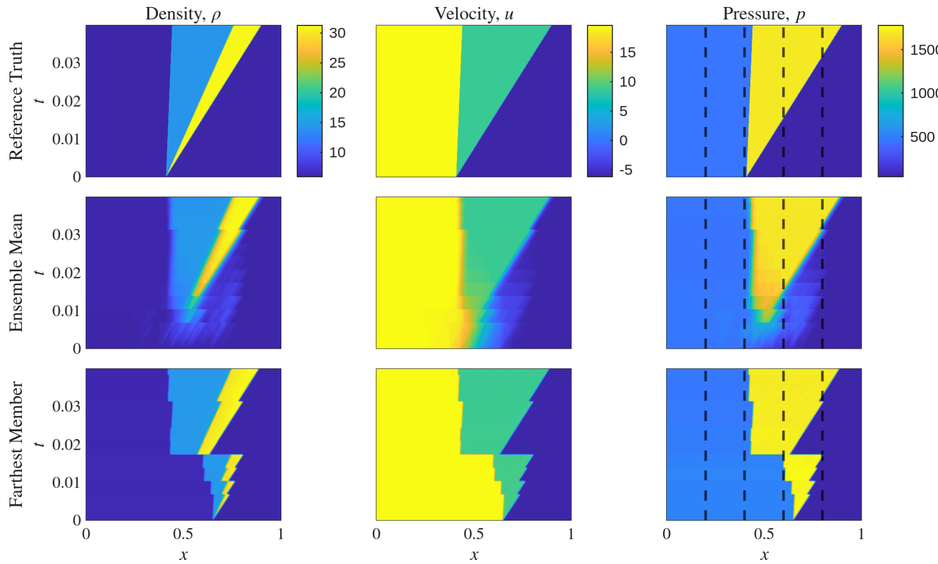

Figure 6: $x - t$ diagrams for Toro's shock tube problem, for the reference truth, ensemble mean, and the farthest ensemble member. The dashed vertical lines represent the pressure sensors.

4.5.2. Shu-Osher Shock-Entropy Problem

Figure 7 demonstrates that the level set EnKF preserves both the sharp shock and the oscillatory features of the entropy wave, while the ensemble converges to the reference truth as the number of DA cycles increases. Figures 8 shows that the ensemble spread remains a similar magnitude to the RMSE, while the x-t diagrams in Figure 9 show improving agreement for both the ensemble mean and the farthest ensemble member.

4.5.3. Sod's Shock Tube Problem

The solution to Sod's shock tube problem comprises a rarefaction wave, a contact surface, and a shock. We represent the shock and contact surface using the level set representation, while we align the rarefaction wave using the affine transformation introduced in Appendix C.6. Figure 10 shows that all features are preserved by the level set EnKF and that the ensemble converges to the reference truth with increasing DA cycle. Figure 11 shows that both RMSE and ensemble spread decrease and remain of similar order. The x-t diagrams in Figure 12 show the ensemble mean and farthest ensemble member approaching the reference solution.

5. Level Set EnKF: 2D Compressible Euler Equations

Subsection 5.1 extends the level set representation to 2D compressible flows, with further details provided in Appendix D. Subsection 5.2 introduces the 2D blast wave problem studied by Subrahmanya and Sandu [27], and Subsection 5.3 demonstrates the level set EnKF for this problem.

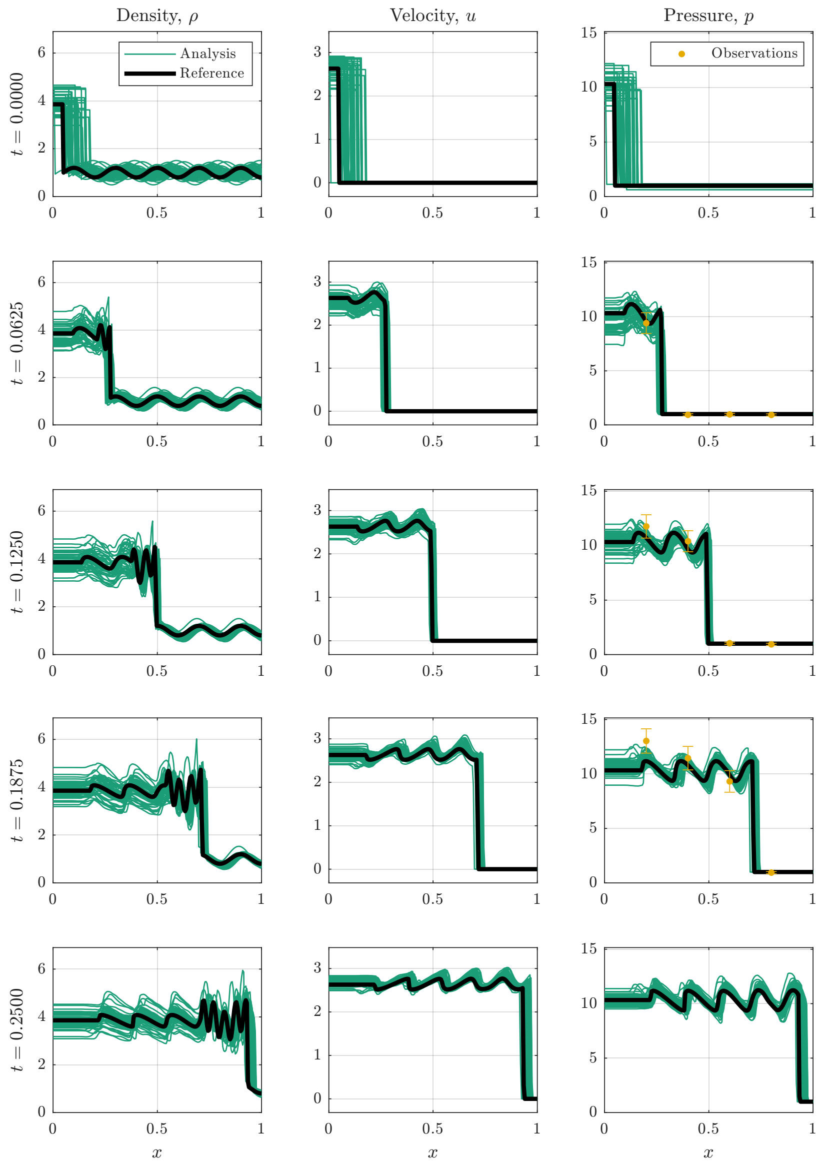

Figure 7: Analysis ensemble for the Shu-Osher shock-entropy problem, plotting the ensemble members against the reference truth immediately following the analysis step, for a subset of DA cycles. With increasing time, the ensemble members show better agreement with the reference truth.

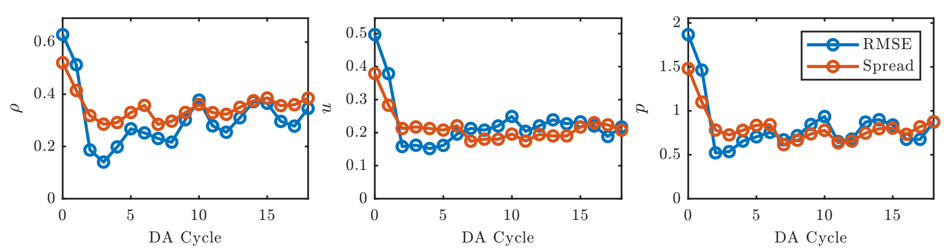

Figure 8: RMSE and spread as a function of DA cycle for the Shu-Osher shock entropy problem. The values at DA cycle 0 correspond to the forecast value before the first DA cycle.

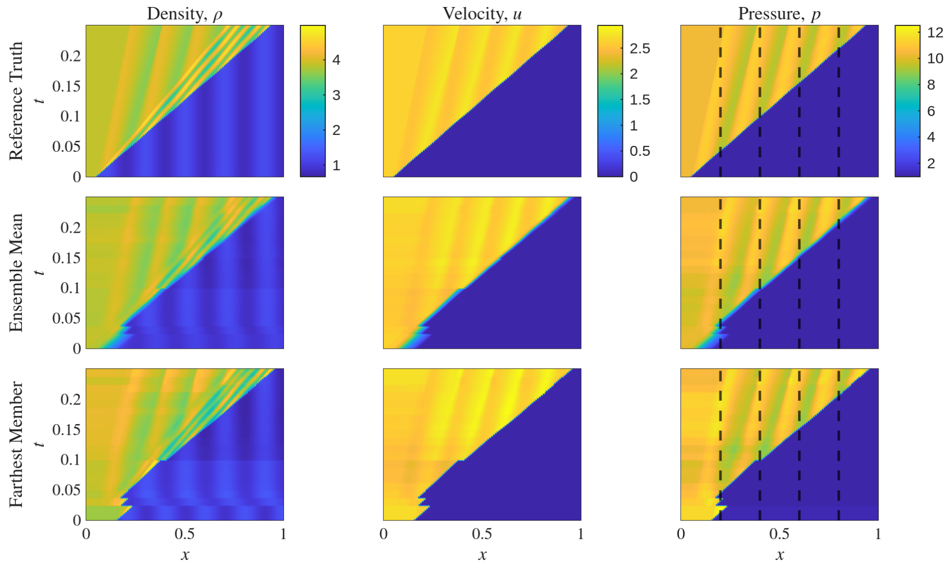

Figure 9: $x - t$ diagrams for the Shu-Osher shock-entropy problem, for the reference truth, ensemble mean, and the farthest ensemble member. The dashed vertical lines represent the pressure sensors.

5.1. 2D Level Set Representation

In 1D, a discontinuity is located at a single point, whereas in 2D it is represented by a curve. Let Γ denote such a curve. The corresponding 2D level set function can be defined as the signed distance function

$$\varphi(\boldsymbol{x}) = \begin{cases} \operatorname{dist}(\boldsymbol{x}, \Gamma), & \boldsymbol{x} \in \Omega_+, \\ -\operatorname{dist}(\boldsymbol{x}, \Gamma), & \boldsymbol{x} \in \Omega_-, \end{cases} \tag{46}$$

where Ω_- denotes the region enclosed by Γ, and Ω_+ denotes the exterior region. Note that the zero level set of $\varphi(\cdot)$ defines the curve Γ. Further details on identifying the zero level set in two dimensions are provided in Appendix D.1.

State extensions are constructed by applying the 1D methodology in the direction normal to the discontinuity. Details of this construction for 2D scalar-valued functions are provided in Appendix D.2, and its extension to the 2D compressible Euler equations is presented in Appendix D.3.

Remark 12. *As discussed in Remark 8, we preserve the shock width imposed by the compressible flow solver and treat the fitted width as a property of the discretization rather than as a state variable. In 1D, we first fit each ensemble member independently. For each primitive field, we take the minimum fitted event width within each member, compute the median of those widths across members, and refit that field in every member with the median width held fixed. In 2D, we first fit the normal-direction profiles for each primitive field in the first ensemble member. We take the median of their fitted widths and refit those profiles, using the median as a prescribed width. We then use the same prescribed width when fitting the remaining ensemble members.*

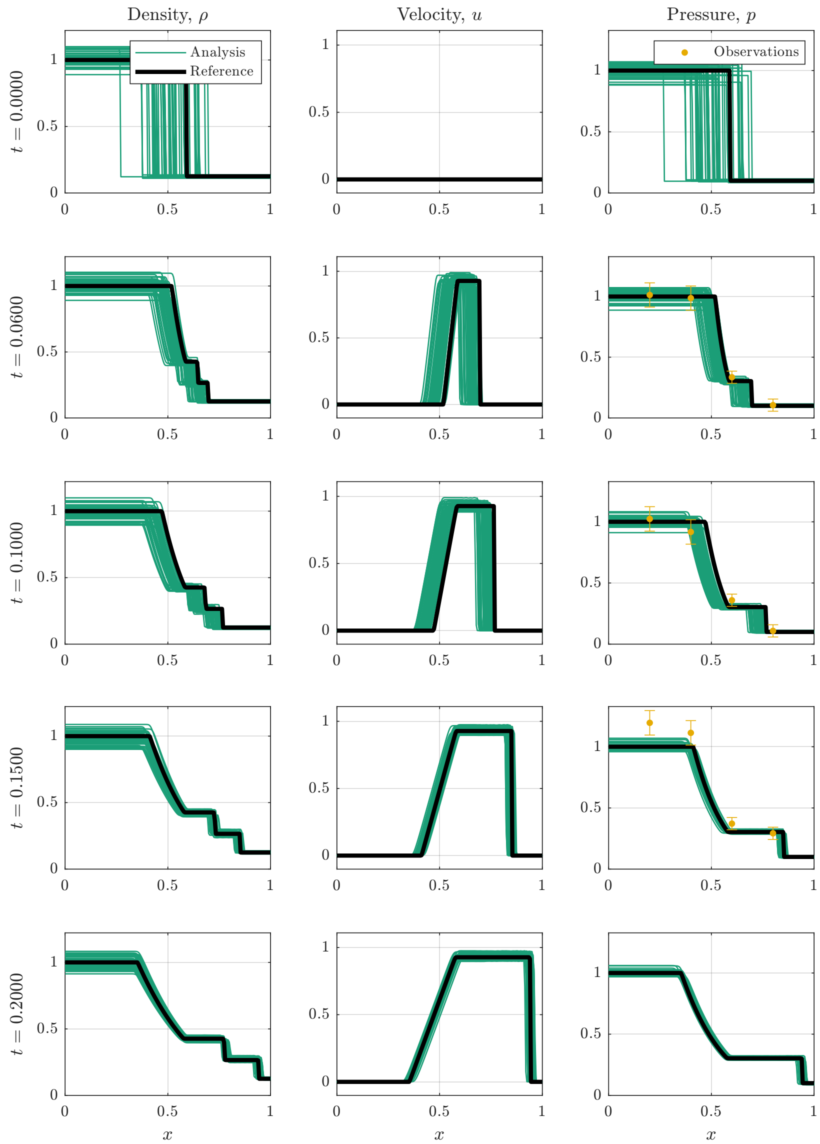

Figure 10: Analysis ensemble for Sod's shock tube problem, plotting the ensemble members against the reference truth immediately following the analysis step, for a subset of DA cycles. With increasing time, the ensemble members show better agreement with the reference truth.

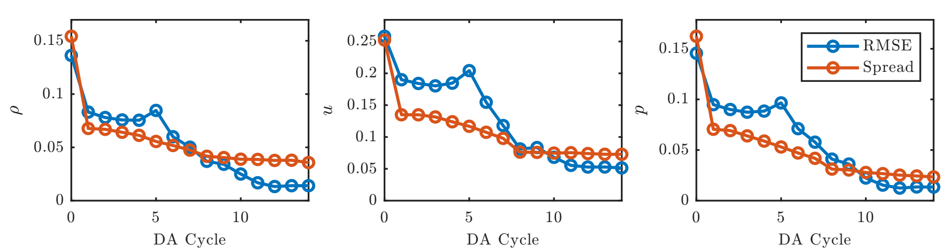

Figure 11: RMSE and spread as a function of DA cycle for Sod's shock tube problem. The values at DA cycle 0 correspond to the forecast value before the first DA cycle.

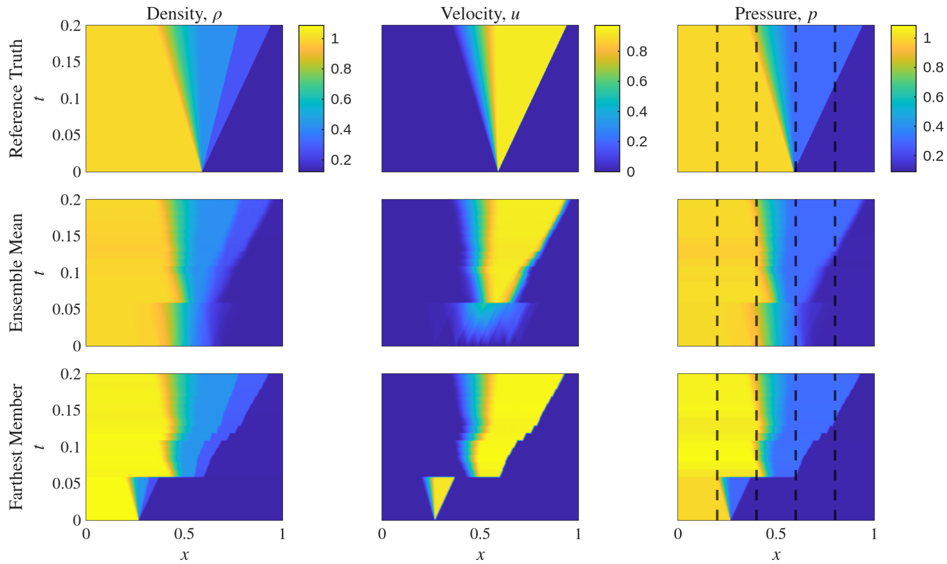

Figure 12: $x - t$ diagrams for Sod's shock tube problem, for the reference truth, ensemble mean, and the farthest ensemble member. The dashed vertical lines represent the pressure sensors.

In 1D, the level set function measures the signed distance to a set of ordered points, whereas in 2D, it encodes the signed distance to curves. If these curves are not aligned, then the signed distance measured by φ will not have a consistent meaning across ensemble members. To demonstrate this, we take the mean of the level set functions φ_1 and φ_2, corresponding to circles whose centers are not aligned. Figure 13 shows that the resulting zero level set is not generally a circle if the circles are not aligned, while aligning them resolves this issue. Therefore, we use a registration procedure, described in Appendix D.4.1, to align the level set functions. Additionally, as in the 1D case, we align rarefaction waves, as described in Appendix D.4.2. We augment the 2D level set representations with the alignment parameters when we apply the transformed EnKF (24).

Remark 13. *Remark 11, we explained that we borrow ideas from image registration [32] to align rarefaction waves in 1D. In 2D, we also use these ideas to align the level set functions. We reiterate that image registration also underlies the morphing EnKF [31].*

5.2. 2D Blast Wave Problem Description

For the square domain $\Omega \equiv [0,2] \times [0,2]$, we introduce the 2D blast wave problem with initial condition

$$\boldsymbol{w}(x) = \begin{cases} \boldsymbol{w}_1 & (x,y) \in \Omega_1, \\ \boldsymbol{w}_2 & (x,y) \in \Omega_2. \end{cases} \tag{47a}$$

for

$$\Omega_1 \equiv \{\boldsymbol{x} \in \Omega | \|\boldsymbol{x} - \boldsymbol{x}_0\|_2 < r\}, \quad \Omega_2 \equiv \Omega \setminus \Omega_1, \tag{47b}$$

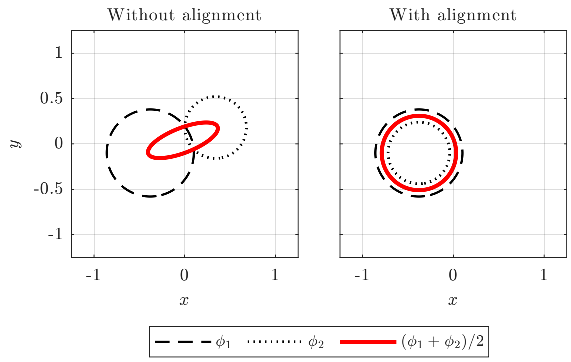

Figure 13: Mean of two circular level set functions, ϕ_1 and ϕ_2 with misaligned centers. The red contours show the zero level sets of $(\phi_1 + \phi_2)/2$. Without alignment, zero level set of the mean is an ellipse. With alignment, it is a circle. Thus, alignment preserves the shape of the original discontinuity curve.

Statistic	x_0	y_0	r	ρ_1	ρ_2	u_1	u_2	p_1	p_2
Truth	1.05	1.05	0.45	1.0	1.0	0	0	1000.0	0.01
μ	1.0	1.0	$r^\dagger$	$\rho_1^\dagger$	$\rho_2^\dagger$	$u_1^\dagger$	$u_2^\dagger$	$p_1^\dagger$	$p_2^\dagger$
σ	0.08	0.08	0.05	0.05	0.05	0	0	100.0	0.001

Table 3: Truth parameters, together with the means and standard deviations used to construct the initial ensemble for the 2D blast wave experiment.

where $\boldsymbol{x} \in \mathbb{R}^2$. We prescribe the interior and exterior states $\boldsymbol{w}_1$ and $\boldsymbol{w}_2$, in terms of the primitive variables $\boldsymbol{w} = (\rho, u, v, p)$. Their values, along with the radius r and center $\boldsymbol{x}_0$ of region Ω_1 are specified in Table 3.

We time march the reference truth solution to $T = 0.025$, depicted in Figure 14a, and compute its level set representation. Figure 14b shows the resulting level set representation of the density field.

5.3. Level Set EnKF for the 2D Blast Wave Problem

As in our 1D examples, uncertainty in the initial condition leads to uncertainty in our state estimate, which we reduce using the level set EnKF. We again assume that the parameters specifying the initial condition are known within error tolerances prescribed in Table 3, and we draw each parameter according to (40). Note that the ensemble means match the truth values for the inner and outer states, while the center of region Ω_1 is offset from the truth.

We generate pressure observations from the reference solution as

$$d_i = p_{\text{ref}}(x_{\text{obs},i}, y_{\text{obs},i}, t; \boldsymbol{q}_1, \boldsymbol{q}_2, x_0, y_0, r) + \eta_i, \quad i = 0, \ldots, N_d - 1, \tag{48}$$

for $\boldsymbol{d} \in \mathbb{R}^{N_d}$, where $\boldsymbol{\eta} \sim \mathcal{N}(0, R)$ for the observation-error covariance R, whose diagonal entries are given by $R_{ii} = \max\{0.1 p_{\text{ref}}(x_{\text{obs},i}, y_{\text{obs},i}, t; \boldsymbol{q}_1, \boldsymbol{q}_2, x_0, y_0, r), 0.05\}$. This choice imposes a relative observation error of 10% and and an absolute error of 0.05. We observe pressure

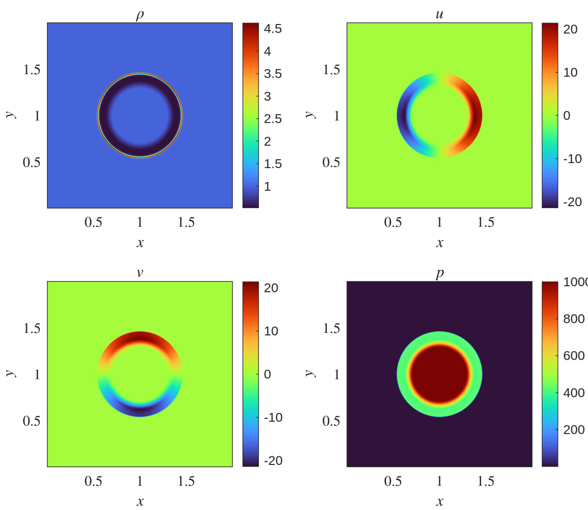

(a) Solution fields.

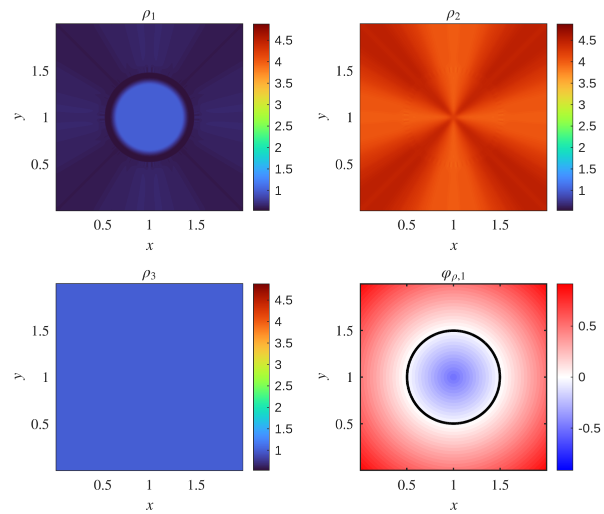

(b) Density level set representation.

Figure 14: Solution and level set representation for the blast wave problem at $T = 0.025$ time units. In (b), the top-left panel shows the region associated with the rarefaction wave, the top-right panel shows the region between the contact and the shock, and the bottom-left panel shows the region outside the shock. The bottom-right panel shows the level set function associated with the contact surface; the black line is its zero level set and therefore identifies the contact-surface location.

on the uniform 4×4 grid so that the full observation set is given by the tensor-product grid

$$(\boldsymbol{x}_{\text{obs}}, \boldsymbol{y}_{\text{obs}}) \in \{0.4, 0.8, 1.2, 1.6\} \times \{0.4, 0.8, 1.2, 1.6\}.$$

Thus, each assimilation cycle uses 16 pressure observations. Figure 15 depicts Ω_1 for each ensemble against the reference truth, as well as the pressure sensors.

The simulation is advanced to $T = 0.01$, with the first observation arriving at $t = 0.0025$ and subsequent DA cycles every $\Delta t_{\text{DA}} = 0.001$. Figure 16 shows the RMSE and ensemble spread as functions of DA cycle. As pressure observations are assimilated, both the RMSE and ensemble spread decrease, indicating that the filter reduces state uncertainty while

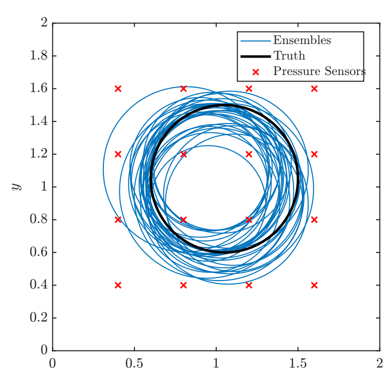

Figure 15: Ensemble of sampled initial discontinuity locations obtained for the blast wave problem, overlayed with the initial discontinuity location for the reference truth and the sensor locations.

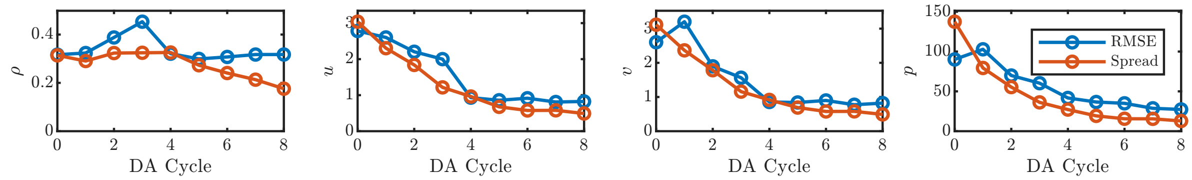

Figure 16: RMSE and spread as a function of DA cycle for the blast wave problem. The density is relatively constant throughout the domain, so the RMSE and spread are both small throughout the whole calculation. The spread and RMSE in the velocity and pressure fields is initially larger, and decreases as more data is assimilated. The spread and RMSE have similar orders of magnitude throughout the calculation. The values at DA cycle 0 correspond to the forecast value before the first DA cycle.

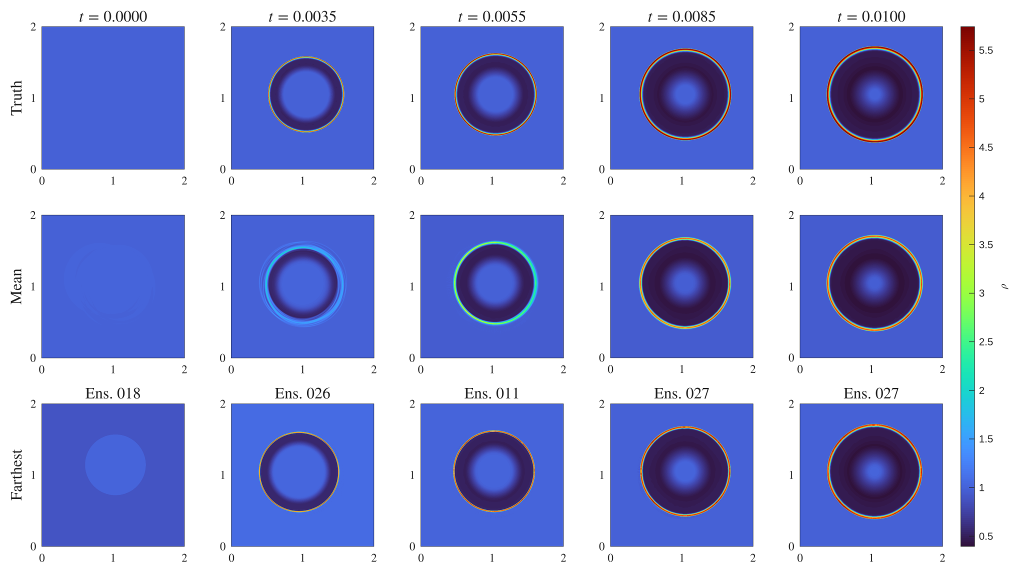

Figure 17: Density field evolution for the 2D blast-wave DA experiment. Columns show selected DA cycles from the initial condition through the final cycle; rows show the truth, ensemble mean, and the farther ensemble member.

maintaining an ensemble spread of the same order as the actual error. The density RMSE and spread remain small throughout the assimilation window because the density field is nearly uniform over the domain.

Figures 17, 18, and 19 plot contours of the density, u-velocity, and pressure, respectively. For each variable, the first row plots the truth, the second row plots the ensemble mean, and the third row plots the farthest ensemble member. We define the farthest ensemble member as described in Subsubsection 4.2.2. For all variables, we observe that the farthest ensemble member moves closer to the reference truth as more data is assimilated, so that the ensemble mean converges to the truth.

6. Conclusion

This paper introduces the *level set EnKF*, which enables sequential DA in compressible flows with shocks and other sharp discontinuities. In this approach, the filter is applied in

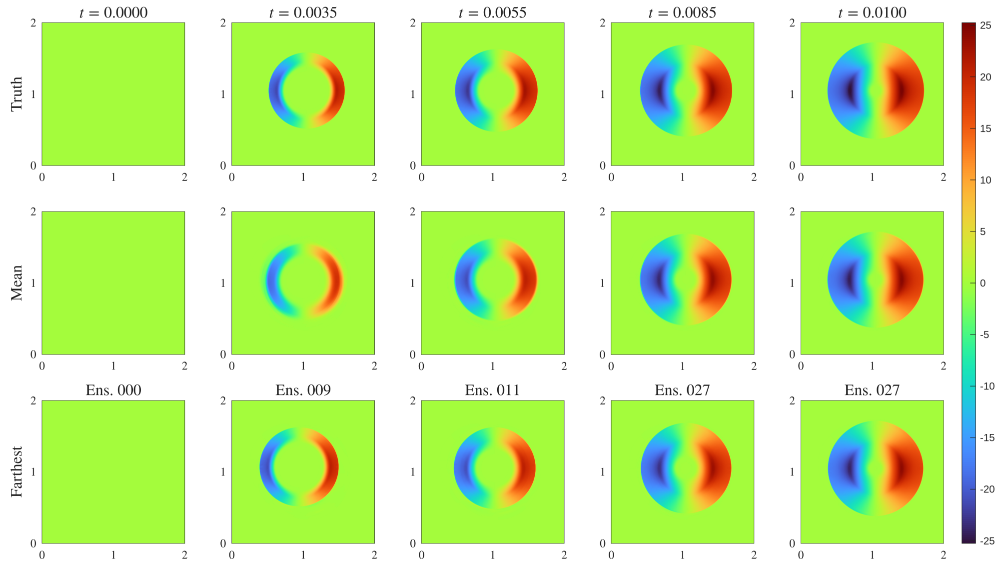

Figure 18: u-velocity field evolution for the 2D blast-wave DA experiment. Columns show selected DA cycles from the initial condition through the final cycle; rows show the truth, ensemble mean, and the farther ensemble member.

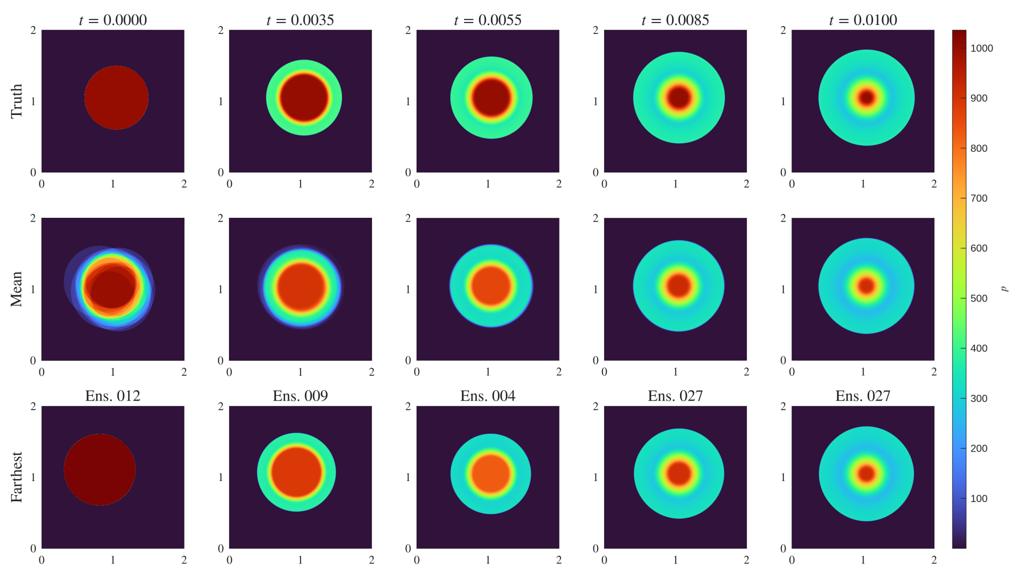

Figure 19: Pressure field evolution for the 2D blast-wave DA experiment. Columns show selected DA cycles from the initial condition through the final cycle; rows show the truth, ensemble mean, and the farther ensemble member.

smooth latent variables, rather than the original state space. The latent variables comprise a level set function that encodes discontinuity location and smooth, globally defined, state extensions, that represent the solution on either side of the discontinuity. By applying the EnKF analysis step in this latent space, rather than directly in state space, the method avoids taking linear combinations of ensemble members with misaligned discontinuities, which is the underlying cause of spurious oscillations introduced by the standard EnKF for these flows.

The level set EnKF is limited by its ability to accurately detect discontinuities, making it less flexible than the morphing EnKF [31] and the neural-network-based approaches [3, 30]. However, its latent space representation is physically interpretable, which is useful for both understanding the action of the filter and incorporating problem-specific inductive bias. In addition, the level set representation explicitly partitions the physical domain into regions associated with distinct flow features. This separation prevents the analysis step from directly coupling regions whose uncertainties are largely unrelated, resonating with other localization techniques that are important in the use of the EnKF [61]. Although the present methodology is limited to relatively simple geometries, it may offer advantages over competing methods when shocks and other sharp interfaces provide a geometrically simple partition of the flow.

More broadly, the level set representation is closely related to methods for shock detection, which remains a challenging post-processing problem in compressible flows. In particular, the methodology introduced in this paper could be used to quantify both shock strength and shock location, as it explicitly identifies a shock location and function values on either side of the shock. Moreover, other shock detection methods could be used to enhance the methodology presented in this paper.

Several limitations remain. The present implementation assumes that the number of discontinuities is known in advance and that each discontinuity can be represented using a hyperbolic tangent function. Extending the method to problems involving more complicated geometries, shock interactions, and intersecting discontinuities will require more flexible procedures for automatic feature identification and latent-space construction. Future work should also investigate more flexible, potentially learned representations of discontinuities as alternatives to the hyperbolic tangent function. Finally, as discussed in Remark 7, more efficient methods for computing or approximating the Jacobians used in the nonlinear least-squares problem should be explored to improve scalability to large-scale problems. These directions are natural next steps toward applying feature-preserving DA to more complex compressible-flow problems.

Code availability

All code used to generate the results and figures presented in this paper is publicly available at https://github.com/mkesleem/LevelSetEnKF.

Data availability

Data will be made available on request.

Declaration of AI Use

Codex was used to improve the efficiency and parallelism of the code for computing the level set representation, improve the readability of the manuscript figures, and create tables for the manuscript. The authors reviewed and verified all AI-assisted changes and take full responsibility for the accuracy, originality, and integrity of the manuscript.

Declaration of competing interest

The authors declare that they have no known competing financial interests or personal relationships that could have appeared to influence the work reported in this paper.

Acknowledgments

This work was supported by the AFOSR/AFRL Center of Excellence in Assimilation of Flow Features in Compressible Reacting Flows (Grant No. FA9550-25-1-0011). Matthias Morzfeld is also supported by the U.S. ONR Grant N000142512298.

References

[1] T. Houba, A. Edoh, R. Munipalli, M. E. Harvazinski, Sequential data assimilation in flows with shocks, in: AIAA SCITECH 2024 Forum, 2024. doi:10.2514/6.2024-0587.

[2] A. Edoh, T. Houba, R. Munipalli, M. E. Harvazinski, Sequential ensemble Kalman filtering of compressible flows with shocks: Enforcing positivity, in: AIAA SCITECH 2025 Forum, 2025. doi:10.2514/6.2025-0918.

[3] X.-H. Zhou, L. Beronilla, M. K. Sleeman, H. Hu, M. Morzfeld, A. M. Stuart, T. A. Zaki, Neural ensemble Kalman filter: Data assimilation for compressible flows with shocks, Journal of Computational Physics 564 (2026) 115136. doi:10.1016/j.jcp.2026.115136.

[4] G. Evensen, Data assimilation: The ensemble Kalman filter, Springer Science & Business Media, 2009.

[5] S. Reich, C. Cotter, Probabilistic forecasting and Bayesian data assimilation, Cambridge University Press, 2015.

[6] E. Kalnay, Atmospheric Modeling, Data Assimilation and Predictability, Cambridge University Press, 2002.

[7] A. J. Majda, J. Harlim, Filtering Complex Turbulent Systems, Cambridge University Press, 2012.

[8] D. S. Oliver, A. C. Reynolds, N. Liu, Inverse theory for petroleum reservoir characterization and history matching, Cambridge University Press, 2008.

[9] A. Carrassi, M. Bocquet, L. Bertino, G. Evensen, Data assimilation in the geosciences: An overview of methods, issues, and perspectives, WIREs Climate Change 9 (5) (2018). doi:10.1002/wcc.535.

[10] X.-L. Zhang, H. Xiao, X. Luo, G. He, Ensemble Kalman method for learning turbulence models from indirect observation data, Journal of Fluid Mechanics 949 (2022) A26.

[11] X.-H. Zhou, H. Wang, J. McClure, C. Chen, H. Xiao, Inference of relative permeability curves in reservoir rocks with ensemble Kalman method, The European Physical Journal E 46 (6) (2023) 44.

[12] M. I. Zafar, X.-H. Zhou, C. J. Roy, D. Stelter, H. Xiao, Data-driven turbulence modeling approach for cold-wall hypersonic boundary layers, Journal of Thermophysics and Heat Transfer 40 (2) (2026) 379–395.

[13] Z. Liu, H. Wang, Z. Zhao, H. Xiao, Toward a unified data-driven turbulence model through multi-objective learning, National Science Review 13 (16) (2026) nwag344. doi:10.1093/nsr/nwag344.

[14] M. Wang, T. A. Zaki, State estimation in turbulent channel flow from limited observations, Journal of Fluid Mechanics 917 (2021) A9.

[15] T. A. Zaki, M. Wang, Chapter 4 - Data assimilation and flow estimation, in: K. Duraisamy (Ed.), Data Driven Analysis and Modeling of Turbulent Flows, Computation and Analysis of Turbulent Flows, Academic Press, 2025, pp. 129–181. doi:10.1016/B978-0-32-395043-5.00010-3.

[16] T. A. Zaki, Turbulence from an observer perspective, Annual Review of Fluid Mechanics 57 (Volume 57, 2025) (2025) 311–334.

[17] D. A. Buchta, T. A. Zaki, Observation-infused simulations of high-speed boundary-layer transition, Journal of Fluid Mechanics 916 (2021) A44.

[18] D. A. Buchta, S. J. Laurence, T. A. Zaki, Assimilation of wall-pressure measurements in high-speed flow over a cone, Journal of Fluid Mechanics 947 (2022) R2.

[19] P. Morra, C. Meneveau, T. A. Zaki, ML for fast assimilation of wall-pressure measurements from hypersonic flow over a cone, Scientific Reports 14 (1) (2024) 12853.

[20] Q. Wang, T. A. Zaki, Domain of dependence for wall-pressure measurements in high-speed boundary layers, Journal of Fluid Mechanics 1009 (2025) A67.

[21] A. Doucet, N. De Freitas, N. Gordon, An introduction to sequential Monte Carlo methods, in: Sequential Monte Carlo methods in practice, Springer, 2001, pp. 3–14.

[22] P. J. van Leeuwen, Particle filtering in geophysical systems, Monthly Weather Review 137 (12) (2009) 4089 – 4114. doi:10.1175/2009MWR2835.1.

[23] M. Arulampalam, S. Maskell, N. Gordon, T. Clapp, A tutorial on particle filters for online nonlinear/non-gaussian bayesian tracking, IEEE Transactions on Signal Processing 50 (2) (2002) 174–188. doi:10.1109/78.978374.

[24] C. Snyder, T. Bengtsson, P. Bickel, J. Anderson, Obstacles to high-dimensional particle filtering, Monthly Weather Review 136 (12) (2008) 4629 – 4640. doi:10.1175/2008MWR2529.1.

[25] C. Snyder, T. Bengtsson, M. Morzfeld, Performance bounds for particle filters using the optimal proposal, Monthly Weather Review 143 (11) (2015) 4750 – 4761. doi:10.1175/MWR-D-15-0144.1.

[26] G. Evensen, Sequential data assimilation with a nonlinear quasi-geostrophic model using Monte Carlo methods to forecast error statistics, Journal of Geophysical Research: Oceans 99 (C5) (1994) 10143–10162.

[27] A. N. Subrahmanya, A. Sandu, Feature preserving data assimilation via feature alignment, Computer Methods in Applied Mechanics and Engineering 447 (2025). doi:10.1016/j.cma.2025.118345.

[28] S. Reich, A nonparametric ensemble transform method for Bayesian inference, SIAM Journal on Scientific Computing 35 (4) (2013) A2013–A2024. doi:10.1137/130907367.

[29] H. Sakoe, S. Chiba, Dynamic programming algorithm optimization for spoken word recognition, IEEE Transactions on Acoustics, Speech, and Signal Processing 26 (1) (1978) 43–49. doi:10.1109/TASSP.1978.1163055.

[30] H. Chandravamsi, H. Hu, P. Thiagarajan, T. A. Zaki, Feature-preserving latent-EnKF for data assimilation of flows with shocks (2026). arXiv:2606.12559.
URL https://arxiv.org/abs/2606.12559

[31] J. D. Beezley, J. Mandel, Morphing ensemble Kalman filters, Tellus B: Chemical and Physical Meteorology (Jan 2008). doi:10.1111/j.1600-0870.2007.00275.x.

[32] L. G. Brown, A survey of image registration techniques, ACM Comput. Surv. 24 (4) (1992) 325–376. doi:10.1145/146370.146374.
URL 10.1145/146370.146374

[33] H. Hu, T. A. Zaki, Morphing EnKF for compressible flows with shock and boundary uncertainties, manuscript in preparation (2026).

[34] N. K. Chada, M. A. Iglesias, L. Roininen, A. M. Stuart, Parameterizations for ensemble Kalman inversion, Inverse Problems 34 (5) (2018) 055009. doi:10.1088/1361-6420/aab6d9.

[35] P. Thompson, Compressible-fluid Dynamics, Advanced engineering series, McGraw-Hill, 1971.

[36] E. F. Toro, Riemann Solvers and Numerical Methods for Fluid Dynamics: A Practical Introduction, Springer Berlin Heidelberg, 2009. doi:10.1007/b79761.
URL https://doi.org/10.1007/b79761

[37] J. Von Neumann, R. D. Richtmyer, A method for the numerical calculation of hydrodynamic shocks, Journal of Applied Physics 21 (3) (1950) 232–237. doi:10.1063/1.1699639.
URL https://doi.org/10.1063/1.1699639

[38] B. van Leer, Towards the ultimate conservative difference scheme. v. a second-order sequel to godunov's method, Journal of Computational Physics 32 (1) (1979) 101–136. doi:10.1016/0021-9991(79)90145-1.

[39] X.-D. Liu, S. Osher, T. Chan, Weighted essentially non-oscillatory schemes, Journal of Computational Physics 115 (1) (1994) 200–212. doi:10.1006/jcph.1994.1187.

[40] A. Jameson, W. Schmidt, E. Turkel, Numerical solution of the Euler equations by finite volume methods using Runge Kutta time stepping schemes, in: 14th Fluid and Plasma Dynamics Conference, 1981. doi:10.2514/6.1981-1259.
URL https://arc.aiaa.org/doi/abs/10.2514/6.1981-1259

[41] F. Ducros, V. Ferrand, F. Nicoud, C. Weber, D. Darracq, C. Gacherieu, T. Poinsot, Large-eddy simulation of the shock/turbulence interaction, Journal of Computational Physics 152 (2) (1999) 517–549. doi:https://doi.org/10.1006/jcph.1999.6238.

[42] D. Moro, N. C. Nguyen, J. Peraire, Dilation-based shock capturing for high-order methods, International Journal for Numerical Methods in Fluids 82 (7) (2016) 398–416. doi:10.1002/fld.4223.

[43] A. H. Razavi, M. Yano, Registration-based nonlinear model reduction of parametrized aerodynamics problems with applications to transonic Euler and RANS flows, Journal of Computational Physics 521 (2025) 113576. doi:10.1016/j.jcp.2024.113576.

[44] Z. Wu, Y. Xu, W. Wang, R. Hu, Review of shock wave detection method in CFD post-processing, Chinese Journal of Aeronautics 26 (3) (2013) 501–513. doi:10.1016/j.cja.2013.05.001.

[45] D. Lovely, R. Haimes, Shock detection from computational fluid dynamics results, in: 14th AIAA Computational Fluid Dynamics Conference, 1999. doi:10.2514/6.1999-3285.

[46] M. Kanamori, K. Suzuki, Shock wave detection in two-dimensional flow based on the theory of characteristics from CFD data, Journal of Computational Physics 230 (8) (2011) 3085–3092. doi:10.1016/j.jcp.2011.01.007.

[47] T. R. Fujimoto, T. Kawasaki, K. Kitamura, Canny-edge-detection/Rankine-Hugoniot-conditions unified shock sensor for inviscid and viscous flows, Journal of Computational Physics 396 (2019) 264–279. doi:10.1016/j.jcp.2019.06.071.

[48] J. Canny, A computational approach to edge detection, IEEE Transactions on Pattern Analysis and Machine Intelligence PAMI-8 (6) (1986) 679–698. doi:10.1109/TPAMI.1986.4767851.

[49] Y. Liu, Y. Lu, Y. Wang, D. Sun, L. Deng, F. Wang, Y. Lei, A CNN-based shock detection method in flow visualization, Computers & Fluids 184 (2019) 1–9. doi:10.1016/j.compfluid.2019.03.022.

[50] S. Chang, J. Liu, K. Cui, A cluster analysis-based shock wave pattern recognition method for two-dimensional inviscid compressible flows, Journal of Computational Physics 506 (2024) 112946. doi:10.1016/j.jcp.2024.112946.

[51] F. Xiao, Y. Honma, T. Kono, A simple algebraic interface capturing scheme using hyperbolic tangent function, International Journal for Numerical Methods in Fluids 48 (9) (2005) 1023–1040. doi:10.1002/fld.975.

[52] A. Baumgart, G. Beardsell, G. Blanquart, Analytical closure to the spatially-filtered Euler equations for shock-dominated flows, Journal of Computational Physics 477 (2023) 111946. doi:https://doi.org/10.1016/j.jcp.2023.111946.

[53] G. Fukushima, K. Kitamura, Improved hybrid approach of monotonic upstream-centered scheme for conservation laws and discontinuity sharpening technique for steady and unsteady flows, Physics of Fluids 36 (4) (2024) 046110. doi:10.1063/5.0198163.

[54] X. Zhao, W. Ma, S. Islam, A. Narkhede, K. Wang, M2C: An open-source software for multiphysics simulation of compressible multi-material flows and fluid-structure interactions, Computer Physics Communications 321 (2026) 110023. doi:10.1016/j.cpc.2026.110023.

[55] C.-W. Shu, S. Osher, Efficient implementation of essentially non-oscillatory shock-capturing schemes, ii, Journal of Computational Physics 83 (1) (1989) 32–78. doi:10.1016/0021-9991(89)90222-2.

[56] G. A. Sod, A survey of several finite difference methods for systems of nonlinear hyperbolic conservation laws, Journal of Computational Physics 27 (1) (1978) 1–31. doi:10.1016/0021-9991(78)90023-2.

[57] R. E. Kalman, A new approach to linear filtering and prediction problems, Journal of Basic Engineering 82 (1) (1960) 35–45. doi:10.1115/1.3662552.

[58] M. Ghil, S. E. Cohn, J. Tavantzis, K. Bube, E. Isaacson, Applications of estimation theory to numerical weather prediction, in: L. Bengtsson, M. Ghil, E. Källén (Eds.),

Dynamic Meteorology: Data Assimilation Methods, Vol. 36 of Applied Mathematical Sciences, Springer-Verlag, 1981, pp. 139–224.

[59] G. Evensen, The ensemble Kalman filter: Theoretical formulation and practical implementation, Ocean dynamics 53 (4) (2003) 343–367.

[60] M. A. Iglesias, K. J. H. Law, A. M. Stuart, Ensemble Kalman methods for inverse problems, Inverse Problems 29 (4) (2013) 045001. doi:10.1088/0266-5611/29/4/045001.

[61] M. Asch, M. Bocquet, M. Nodet, Data assimilation: methods, algorithms, and applications, SIAM, 2016.

Appendix A. Compressible Euler Equations

This appendix briefly reviews the compressible Euler equations, we refer the reader to [36] for a detailed description. The compressible Euler equations are a system of nonlinear hyperbolic conservation laws that describe the dynamics of a compressible, inviscid flow within the continuum approximation. Such flows can be expressed in terms of the *primitive variables* (ρ, u, v, w, p), where ρ denotes the density, $\boldsymbol{u} = (u, v, w)$ represents the velocity field with components in the x, y, and z directions, respectively, and p is the pressure. Alternatively, the flow can be expressed in terms of the *conservative variables* $(\rho, \rho u, \rho v, \rho w, E)$, where ρ is the density, $\rho\boldsymbol{u} = \rho(u, v, w)$ is the momentum, and E is the total energy

$$E = \rho\Big(e + \frac{\boldsymbol{u}\cdot\boldsymbol{u}}{2}\Big) = \rho\Big(e + \frac{u^2 + v^2 + w^2}{2}\Big) \tag{A.1}$$

while e is the specific internal energy and $(\boldsymbol{u}\cdot\boldsymbol{u})/2$ is the specific kinetic energy. In conservative form, the compressible Euler equations can be written as

$$\frac{\partial \rho}{\partial t} + \nabla\cdot(\rho\boldsymbol{u}) = 0, \tag{A.2a}$$

$$\frac{\partial(\rho\boldsymbol{u})}{\partial t} + \nabla\cdot(\rho\boldsymbol{u}\otimes\boldsymbol{u}) + \nabla p = 0, \tag{A.2b}$$

$$\frac{\partial E}{\partial t} + \nabla\cdot[(E + p)\boldsymbol{u}] = 0. \tag{A.2c}$$

We relate the thermodynamic variables using the ideal gas law

$$p = \rho R T \tag{A.3}$$

while for thermally and calorically perfect gases, we obtain

$$e = c_v T \tag{A.4}$$

where $R = c_p - c_v$ is the specific gas constant, T is the temperature, c_p is the specific heat capacity at constant pressure, and c_v is the specific heat capacity at constant volume. Thus, the pressure can be expressed in terms of the energy and momentum as

$$p = (\gamma - 1)\Big[E - \frac{(\rho\boldsymbol{u}) \cdot (\rho\boldsymbol{u})}{2\rho}\Big], \tag{A.5}$$

where $\gamma = c_p/c_v$ is the specific heat capacity ratio. We write the conservative variables as

$$\boldsymbol{q} = \begin{bmatrix} q_1 \\ q_2 \\ q_3 \\ q_4 \\ q_5 \end{bmatrix} = \begin{bmatrix} \rho \\ \rho u \\ \rho v \\ \rho w \\ E \end{bmatrix}, \tag{A.6a}$$

and the primitive variables as

$$\boldsymbol{w} = \begin{bmatrix} \rho \\ u \\ v \\ w \\ p \end{bmatrix} = \begin{bmatrix} q_1 \\ q_2/q_1 \\ q_3/q_1 \\ q_4/q_1 \\ (\gamma - 1)[q_5 - (q_2^2 + q_3^2 + q_4^2)/(2q_1)] \end{bmatrix}, \tag{A.6b}$$

so that (A.6) describes the conservative-to-primitive transformation.

Appendix B. Interface Sharpening Using the Level Set Representation

Godunov's scheme is a finite volume method for conservation laws. It uses piecewise-constant reconstruction, resulting in a method that is first-order accurate in space and time. Consequently, the scheme introduces significant numerical dissipation. Higher-order methods, such as the MUSCL scheme [38] and the WENO method [39], reduce smearing. MUSCL schemes use piecewise-linear reconstruction and employ *slope limiters* to prevent spurious numerical oscillations, at the expense of smearing of sharp interfaces, albeit, to a lesser degree than Godunov's method [38]. WENO methods use multiple candidate stencils for solution reconstruction and compute nonlinear weights that adaptively reduce the influence of stencils containing discontinuities [39]. WENO methods substantially improve the resolution of shocks, relative to MUSCL and Godunov schemes, yet still introduce some numerical dissipation, which causes sharp interfaces to be smeared over a small number of grid cells.

Our level set representation models shock and contact surfaces using a hyperbolic tangent function with a finite width δ. In principle, we could take the limit $\delta \to 0$ to sharpen these interfaces in the analysis step. However, this would interact unfavorably with the prediction step. In particular, the experiments reported in this paper use the `M2C` code, based on a MUSCL scheme. Introducing sharp discontinuities in the analysis step would effectively undo the smoothing introduced by the slope limiters, which are required to suppress spurious numerical oscillations near discontinuities. Therefore, we fit a finite interface width δ when

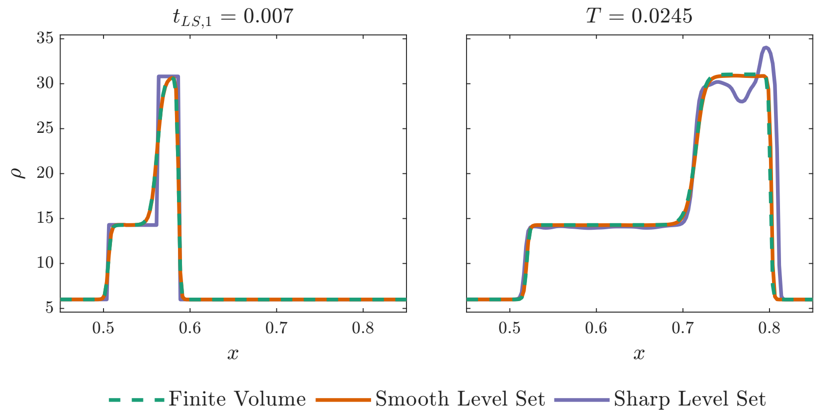

Figure B.20: Evolution of smooth and sharp level set representations of Toro's shock tube solution compared with the reference finite volume solution for the density field.

constructing our level set representation such that δ respects the length scale of the shock introduced by the numerical solver.

Figure B.20 demonstrates the negative impacts of sharpening shocks and contact surfaces using the level set representation. We first march to $t_{LS,1} = 0.007$ and fit a level set representation. Starting from this time, we evolve three solutions: the fitted smooth representation, with δ determined during fitting; the corresponding sharp representation, obtained by taking the limit $\delta \to 0$; and the reference finite volume solution. After each additional interval of $\Delta t = 0.0035$, the level set representations are refitted and evolved again. This process is repeated until the final time $T = 0.0245$. We observe that the sharp representation produces larger oscillations and causes the right-most shock to propagate at an incorrect speed relative to the reference solution, while the fitted smooth representation remains much closer to the reference finite volume solution. This behavior is consistent with the findings of Fukushima and Kitamura [53], which we summarize in Subsubsection 1.2.3.

Appendix C. Implementation Details for 1D Level Set Representations

This appendix provides implementation details for the level set representation of 1D scalar fields introduced in Section 3. Appendix C.1 explains how the optimization problem (33) used to fit the level set reconstruction map (31) can be reformulated as a local minimization problem. The continuous formulation is presented in Appendix C.2, while the corresponding discrete formulation is given in Appendix C.3. Algorithms 1 and 2, presented in Appendix C.3, together define the procedure used to construct a level set representation of a one-dimensional function containing a single discontinuity. Algorithm 3 in Appendix C.4 describes how to extend the procedure to multiple discontinuities based on the discussion in Subsection 3.2. Finally, Appendix C.5 extends the scalar methodology to solutions of the 1D Euler equations.

Appendix C.1. Treatment as a Local Minimization Problem

Although (33) is stated globally, the hyperbolic tangent transition is localized near the discontinuity. For x sufficiently far to the left of x_s, $\tanh((x - x_s)/\delta) \approx -1$, so $\mathcal{T}^{-1}(\boldsymbol{\phi})(x) \approx f_L(x)$. Similarly, for x sufficiently far to the right of x_s, $\tanh((x-x_s)/\delta) \approx 1$, so $\mathcal{T}^{-1}(\boldsymbol{\phi})(x) \approx f_R(x)$. Thus, the transition from f_L to f_R is confined to a neighborhood of x_s, and we can restrict the minimization problem to this neighborhood. We identify this neighborhood using the local minima of $|f'(x)|$ to the left and right of the discontinuity.

Appendix C.2. Continuous Formulation of the Local Minimization Problem

To localize the minimization problem, we estimate the discontinuity location as

$$x_{s,0} = \arg\max_{x\in\Omega} |f'(x)|. \tag{C.1}$$

We then identify local minima of $|f'(x)|$ to the left and right of $x_{s,0}$, denoted $x_{s,L}$ and $x_{s,R}$, respectively. The localized minimization problem is solved over $\Omega_{\text{loc}} \equiv [x_{s,L}, x_{s,R}]$ as

$$\boldsymbol{\phi}_{\text{loc},*} = \arg\min_{\boldsymbol{\phi}\in\mathcal{X}_{\text{loc}}} J_{\text{loc}}(\boldsymbol{\phi}; f), \tag{C.2a}$$

with objective function

$$\begin{aligned} J_{\text{loc}}(\boldsymbol{\phi}; f) = &\int_{\Omega_{\text{loc}}} \left|\mathcal{T}^{-1}(\boldsymbol{\phi})(x) - f(x)\right|^2 dx \\ &+ \lambda_1 \int_{\Omega_{\text{loc}}} \left(|f_L'(x)|^2 + |f_R'(x)|^2\right) dx \\ &+ \lambda_b(|f_L(x_{s,L}) - f(x_{s,L})|^2 + |f_R(x_{s,R}) - f(x_{s,R})|^2) \end{aligned} \tag{C.2b}$$

where

$$\mathcal{X}_{\text{loc}} = C^1(\Omega_{\text{loc}}) \times C^1(\Omega_{\text{loc}}) \times \Omega_{\text{loc}} \times \mathbb{R}_{>0}. \tag{C.2c}$$

The term proportional to λ_b penalizes violations of the boundary values at the ends of the localized region.

Solving (C.2) gives the localized solution

$$\boldsymbol{\phi}_{\text{loc},*} = (f_{\text{loc,L},*}, f_{\text{loc,R},*}, x_{s,*}, \delta_*). \tag{C.3}$$

Outside Ω_{loc}, we keep the extension associated with the physical side equal to the original function and hold the opposite extension constant at the nearest fitted endpoint as

$$f_{L,*}(x) = \begin{cases} f(x) & x < x_{s,L}, \\ f_{\text{loc,L},*}(x) & x_{s,L} \le x < x_{s,R}, \\ f_{\text{loc,L},*}(x_{s,R}) & x_{s,R} \le x, \end{cases} \tag{C.4a}$$

$$f_{R,*}(x) = \begin{cases} f_{\text{loc,R},*}(x_{s,L}) & x < x_{s,L}, \\ f_{\text{loc,R},*}(x) & x_{s,L} \le x < x_{s,R}, \\ f(x) & x_{s,R} \le x. \end{cases} \tag{C.4b}$$

Appendix C.3. Discrete Formulation of the Local Minimization Problem

In practice, we apply the preceding construction to values of f on a finite grid. Let $x_i \in \Omega$, $i = 1, \ldots, N_x$, denote a uniform grid of cell centers with spacing Δx, and let $\boldsymbol{f} \in \mathbb{R}^{N_x}$ denote the corresponding value at the cell centers. We approximate the derivative using a finite-difference matrix $D \in \mathbb{R}^{N_x \times N_x}$, so that $D\boldsymbol{f}$ approximates f' on the grid. The discrete estimate of the discontinuity location is

$$i_{s,0} = \operatorname*{arg\,max}_{i=1,\ldots,N_x} |[D\boldsymbol{f}]_i|, \qquad x_{s,0} = x_{i_{s,0}}. \tag{C.5}$$

We then identify indices $i_{s,L} < i_{s,0}$ and $i_{s,R} > i_{s,0}$ corresponding to local minima of $|D\boldsymbol{f}|$ to the left and right of $i_{s,0}$, respectively. This defines the local index set

$$\mathcal{I}_{\text{loc}} = \{i_{s,L}, i_{s,L}+1, \ldots, i_{s,R}\}, \tag{C.6}$$

with

$$\boldsymbol{\phi}_h = (\boldsymbol{f}_L, \boldsymbol{f}_R, x_s, \delta) \in \mathbb{R}^{N_{\text{loc}}} \times \mathbb{R}^{N_{\text{loc}}} \times [x_{i_{s,L}}, x_{i_{s,R}}] \times \mathbb{R}_{>0}, \tag{C.7}$$

where $N_{\text{loc}} = |\mathcal{I}_{\text{loc}}|$ and $\boldsymbol{f}_L, \boldsymbol{f}_R$ denote the local grid values of the left and right state extensions. For $i \in \mathcal{I}_{\text{loc}}$, the discrete reconstruction is

$$\left[\mathcal{T}_h^{-1}(\boldsymbol{\phi}_h)\right]_i = \frac{f_{L,i} + f_{R,i}}{2} - \frac{f_{L,i} - f_{R,i}}{2} \tanh\left(\frac{x_i - x_s}{\delta}\right). \tag{C.8}$$

We approximate the continuous objective (C.2) by

$$\boldsymbol{\phi}_{h,*} = \operatorname*{arg\,min}_{\boldsymbol{\phi}_h \in \mathcal{X}_{\text{loc},h}} J_{\text{loc},h}(\boldsymbol{\phi}_h; \boldsymbol{f}), \tag{C.9a}$$

with

$$\begin{aligned} J_{\text{loc},h}(\boldsymbol{\phi}_h; \boldsymbol{f}) = \Delta x &\sum_{i \in \mathcal{I}_{\text{loc}}} \left| \left[\mathcal{T}_h^{-1}(\boldsymbol{\phi}_h)\right]_i - f_i \right|^2 \\ &+ \lambda_1 \Delta x \left(\|D_{\text{loc}} \boldsymbol{f}_L\|_2^2 + \|D_{\text{loc}} \boldsymbol{f}_R\|_2^2\right) \\ &+ \lambda_b \left(|f_{i_{s,L}} - f_{L,i_{s,L}}|^2 + |f_{i_{s,R}} - f_{R,i_{s,R}}|^2\right), \end{aligned} \tag{C.9b}$$

where

$$\mathcal{X}_{\text{loc},h} = \mathbb{R}^{N_{\text{loc}}} \times \mathbb{R}^{N_{\text{loc}}} \times [x_{i_{s,L}}, x_{i_{s,R}}] \times \mathbb{R}_{>0}. \tag{C.9c}$$

Here D_{loc} is the finite-difference matrix restricted to the local grid. Note that boundary differences inherit the global stencil and can be computed from the global solution. Further note that, for notational convenience, entries of local vectors are indexed by their corresponding global grid indices.

We solve (C.9) a bound-constrained trust-region reflective nonlinear least-squares method, with the Jacobian approximated using two-point finite differences (see Subsubsection 3.1.1). We initialize the solver with $\delta_0 = \Delta x$, $x_{s,0}$ computed using (C.5), and

$$f_{L,0,i} = \begin{cases} f_i & i \le i_{s,L}, \\ f_{i_{s,L}} & i > i_{s,L}, \end{cases} \quad f_{R,0,i} = \begin{cases} f_{i_{s,R}} & i < i_{s,R}, \\ f_i & i \ge i_{s,R}, \end{cases} \tag{C.10}$$

for $i \in \mathcal{I}_{\text{loc}}$. We summarize this initialization procedure in Algorithm 1.

Algorithm 1: Initialization of the 1D Level Set Representation

Input: $\boldsymbol{x}$ and $\boldsymbol{f}$

Output: Initial local extensions $\boldsymbol{f}_{L,0}$, $\boldsymbol{f}_{R,0}$, discontinuity estimate $x_{s,0}$, endpoint indices $i_{s,L}$ and $i_{s,R}$, and local index set $\mathcal{I}_{\text{loc}}$.

Compute $D\boldsymbol{f}$;
Compute $i_{s,0}$ and $x_{s,0}$ using (C.5);
Identify $i_{s,L} < i_{s,0}$ and $i_{s,R} > i_{s,0}$ as local minima of $|D\boldsymbol{f}|$;
Set $\mathcal{I}_{\text{loc}} = \{i_{s,L}, i_{s,L}+1, \ldots, i_{s,R}\}$;
Compute $\boldsymbol{f}_{L,0}$ and $\boldsymbol{f}_{R,0}$ using (C.10);

Solving (C.9) gives $\boldsymbol{\phi}_{h,*} = (\boldsymbol{f}_{\text{loc},L,*}, \boldsymbol{f}_{\text{loc},R,*}, x_{s,*}, \delta_*)$ on the local grid. As in the continuous setting, outside the local interval the physical-side extension is set equal to the original grid data and the opposite extension is held constant so that

$$f_{L,*,i} = \begin{cases} f_i & i < i_{s,L}, \\ f_{\text{loc},L,*,i} & i_{s,L} \le i \le i_{s,R}, \\ f_{\text{loc},L,*,i_{s,R}} & i > i_{s,R}, \end{cases} \tag{C.11a}$$

$$f_{R,*,i} = \begin{cases} f_{\text{loc},R,*,i_{s,L}} & i < i_{s,L}, \\ f_{\text{loc},R,*,i} & i_{s,L} \le i \le i_{s,R}, \\ f_i & i > i_{s,R}. \end{cases} \tag{C.11b}$$

The full discrete level set construction is summarized in Algorithm 2.

Algorithm 2: Optimization of the 1D Level Set Representation

Input: $\boldsymbol{x}$, $\boldsymbol{f}$, λ_1, and λ_b

Output: Full-grid level set variables $\boldsymbol{f}_{L,*}$, $\boldsymbol{f}_{R,*}$, $x_{s,*}$, and δ_*.

Run Algorithm 1 to obtain $\boldsymbol{f}_{L,0}$, $\boldsymbol{f}_{R,0}$, $x_{s,0}$, $i_{s,L}$, $i_{s,R}$, and $\mathcal{I}_{\text{loc}}$;
Set the initial width $\delta_0 = \Delta x$;
Form $\boldsymbol{\phi}_{h,0} = (\boldsymbol{f}_{L,0}, \boldsymbol{f}_{R,0}, x_{s,0}, \delta_0)$ on $\mathcal{I}_{\text{loc}}$;
Solve (C.9), initialized with $\boldsymbol{\phi}_{h,0}$, to obtain $\boldsymbol{\phi}_{h,*} = (\boldsymbol{f}_{\text{loc},L,*}, \boldsymbol{f}_{\text{loc},R,*}, x_{s,*}, \delta_*)$;
Extend $\boldsymbol{f}_{\text{loc},L,*}$ and $\boldsymbol{f}_{\text{loc},R,*}$ to the full grid using (C.11);

Remark 14. *After solving the optimization problem* (C.9)*, we can optionally enforce monotonicity of* $\boldsymbol{f}_{\text{loc},L}$ *and* $\boldsymbol{f}_{\text{loc},R}$ *to suppress spurious local oscillations in the reconstructed states.*

Appendix C.4. 1D Level Set Representation for a Scalar Field with Multiple Discontinuities: Implementation Details

Here we extend the 1D level set representation methodology for scalar functions with a single discontinuity to 1D scalar functions with multiple discontinuities. Appendix C.1 argues that we can fit the reconstruction map (31) by solving (33) as a local, rather than a global, minimization problem because the hyperbolic tangent function transitions between its extreme values so quickly. Making a similar argument, we can solve independent local minimization problems to fit the reconstruction map for solutions with multiple discontinuities.

First, we estimate the center of each discontinuity from local maxima of $|D\boldsymbol{f}|$. For each estimated center, we choose a local neighborhood bounded by nearby local minima of $|D\boldsymbol{f}|$, truncating the neighborhood if necessary so that it contains no other discontinuity center. We then solve an independent local minimization problem for each discontinuity, as outlined in Algorithm 3. When neighboring discontinuities are too close to admit non-overlapping local neighborhoods, the corresponding events can instead be fit simultaneously by solving a joint local optimization problem.

Algorithm 3: Local fitting of the level set representation with multiple discontinuities

---

Input: $\boldsymbol{x}$ and $\boldsymbol{f}$, number of discontinuities K, regularization parameters λ_1 and λ_b.
Output: Level set variables $\{\boldsymbol{f}_{L,k,*}, \boldsymbol{f}_{R,k,*}, x_{s,k,*}, \delta_{k,*}\}_{k=1}^{K}$.

Compute $D\boldsymbol{f}$;
Identify K local maxima of $|D\boldsymbol{f}|$ with indices $i_{s,1}, \ldots, i_{s,K}$;
Sort the indices so that $x_{i_{s,1}} < x_{i_{s,2}} < \cdots < x_{i_{s,K}}$;
for $k = 1, \ldots, K$ **do**
  Select a local neighborhood containing $i_{s,k}$ and no other discontinuity centers;
  Restrict $\boldsymbol{f}$ and $\boldsymbol{x}$ to this neighborhood;
  Run Algorithm 1 on the restricted data to obtain $\boldsymbol{f}_{L,k,0}$, $\boldsymbol{f}_{R,k,0}$, $x_{s,k,0}$, $i_{s,k,L}$, $i_{s,k,R}$, and $\mathcal{I}_{\mathrm{loc},k}$;
  Set $\delta_{k,0} = \Delta x$;
  Form $\boldsymbol{\phi}_{h,k,0} = (\boldsymbol{f}_{L,k,0}, \boldsymbol{f}_{R,k,0}, x_{s,k,0}, \delta_{k,0})$ on $\mathcal{I}_{\mathrm{loc},k}$;
  Solve (C.9), initialized with $\boldsymbol{\phi}_{h,k,0}$, to obtain $\boldsymbol{\phi}_{h,k,*} = (\boldsymbol{f}_{\mathrm{loc},k,L,*}, \boldsymbol{f}_{\mathrm{loc},k,R,*}, x_{s,k,*}, \delta_{k,*})$;
  Extend $\boldsymbol{f}_{\mathrm{loc},k,L,*}$ and $\boldsymbol{f}_{\mathrm{loc},k,R,*}$ to the full grid using (C.11);
  Store $(\boldsymbol{f}_{L,k,*}, \boldsymbol{f}_{R,k,*}, x_{s,k,*}, \delta_{k,*})$;

Appendix C.5. Level Set Representation for 1D Compressible Euler Equations

Here we extend the level set representation for scalar functions to vector-valued functions, such as those obtained from solutions to the 1D Euler equations. For a single flow field $\boldsymbol{w} = (\rho, u, p)$, we apply the level set representation method field-by-field, as shown in Algorithm 4.

To avoid updating the shock width during the EnKF analysis step, we fit level set representations such that all ensemble members use the same event widths. First, we fit a level set representation to each ensemble member separately, and then to refit the level set representation for all ensemble members using the median shock width, as outlined in Algorithm 5.

Appendix C.6. Affine Alignment of Smoothly Varying Features

The hyperbolic tangent function can be used to model sharp features. However, it is not suitable to model features that are slowly and continuously varying, such as a rarefaction

Algorithm 4: Level set representation for a single 1D flow

Input: Primitive fields $\boldsymbol{w} = (\rho, u, p)$, expected discontinuity counts $\boldsymbol{K}$, and optionally prescribed shock widths $\boldsymbol{\delta}_{\mathrm{c}} = (\delta_{\rho,\mathrm{c}}, \delta_{u,\mathrm{c}}, \delta_{p,\mathrm{c}})$.
Output: Level set representation

for *each field* w_i *with* $K_i > 0$ **do**
  if $\delta_{\mathrm{c},i}$ *is not prescribed* **then**
    Apply Algorithm 3 to w_i;
  else
    Apply Algorithm 3 to w_i with prescribed $\delta_{\mathrm{c},i}$;

Algorithm 5: Level set representation for an ensemble of 1D flows

Input: Primitive-field ensemble $\{\boldsymbol{w}^{(n)}\}_{n=1}^{N_e}$ and expected discontinuity counts $\boldsymbol{K}$.
Output: Ensemble of level set representations, fitted with common widths.

for $n = 1, \ldots, N_e$ **do**
  Apply Algorithm 4 to $\boldsymbol{w}^{(n)}$ without prescribed widths and obtain $\boldsymbol{\delta}^{(n)}$;
for *each field* w_i *with* $K_i > 0$ **do**
  Set $\delta_{c,i} = \mathrm{median}_{1 \leq n \leq N_e} \, \delta_i^{(n)}$;
for $n = 1, \ldots, N_e$ **do**
  Apply Algorithm 4 to $\boldsymbol{w}^{(n)}$ with prescribed field widths $\boldsymbol{\delta}_c$;

wave in a compressible flow. Although rarefaction waves vary continuously, and slowly compared to shocks and contact surfaces, we observe that the standard EnKF still performs poorly for these features. Therefore, we additionally handle rarefaction waves by aligning them using an affine transformation in x.

Let us denote this transformation by

$$\mathcal{R}_{(a,b)}(f)(x) = f(ax+b), \tag{C.12a}$$

with inverse

$$\mathcal{R}^{-1}_{(a,b)}(f)(x) = f((x-b)/a), \tag{C.12b}$$

where we restrict to $a > 0$ so that the spatial map is invertible and orientation preserving. To align $f^{(2)}(x)$ with $f^{(1)}(x)$, we compute

$$s^{(1)}(x) = \left|\frac{df^{(1)}}{dx}\right|, \quad s^{(2)}(x) = \left|\frac{df^{(2)}}{dx}\right|, \tag{C.13a}$$

which we normalize as

$$s^{(1)*}(x) = \frac{s^{(1)}(x)}{\max_{x\in\mathcal{D}} s^{(1)}(x)}, \quad s^{(2)*}(x) = \frac{s^{(2)}(x)}{\max_{x\in\mathcal{D}} s^{(2)}(x)}. \tag{C.13b}$$

Then we solve the minimization problem

$$(a,b) = \underset{a\in\mathbb{R}_{>0}, b\in\mathbb{R}}{\arg\min} \|s^{(1)*}(x) - \mathcal{R}_{(a,b)}(s^{(2)*})\|_2^2, \tag{C.13c}$$

which minimizes the difference in their normalized gradients. This affine transformation is similar to the registration procedure employed by the morphing EnKF [31], but it comprises only two parameters, and is thus much simpler.

Appendix D. Implementation Details for 2D Level Set Representations

This Appendix presents details on identifying the level set representation for 2D compressible flows. Appendix D.1 describes how to identify the zero level set for a discontinuity in 2D, and how to subsequently construct the level set function.

Appendix D.1. Identifying the Zero Level Set of a 2D Scalar Field

For 1D scalar field, we obtain an initial estimate of the discontinuity location by identifying local maxima of the solution gradient, as described in Appendix C.2. This subsection extends the procedure to a 2D scalar field.

Consider the domain $\Omega \subset \mathbb{R}^2$ with coordinate $\boldsymbol{x} \in \mathbb{R}^2$. Let $f : \Omega \to \mathbb{R}$ denote a 2D scalar field, and let us assume that there exists a discontinuity of f in Ω. Let $\boldsymbol{X}(s)$ denote a set of points along this discontinuity, parameterized by arc length s. For closed curves, $\boldsymbol{X}(s)$ is periodic with period L, and we need only consider $s \in [0, L)$. From this, we obtain the curve

$$\Gamma \equiv \{\boldsymbol{X}(s) : s \in [0, L)\}, \tag{D.1}$$

The gradient of f

$$\nabla f = (\partial_x f, \partial_y f), \tag{D.2}$$

and its norm

$$s_1(\boldsymbol{x}) = \|\nabla f(\boldsymbol{x})\|_2, \tag{D.3}$$

will be large near Γ. Thus, we identify the point

$$\boldsymbol{x}_{s,0} = \arg\max_{\boldsymbol{x}\in\Omega} s_1(\boldsymbol{x}), \tag{D.4}$$

where the gradient norm is maximal, and we take this to be the first point in our discontinuity curve, so that

$$\Gamma_0 \equiv \{x_{s,0}\}. \tag{D.5}$$

The gradient of f is locally normal the discontinuity curve, so the local unit tangent vector is

$$\boldsymbol{t}(\boldsymbol{x}) = \frac{1}{\|\nabla f(\boldsymbol{x})\|_2}\begin{bmatrix}-\partial_y f(\boldsymbol{x})\\ \partial_x f(\boldsymbol{x})\end{bmatrix}. \tag{D.6}$$

We seek the next point on the discontinuity curve by maximizing the gradient magnitude along the tangent direction $\boldsymbol{t}$. Given the current point $\boldsymbol{x}_{s,i}$, we compute

$$\boldsymbol{x}_{s,i+1} = \arg\max_{\boldsymbol{x}\in\{\boldsymbol{x}_{s,i}+r\boldsymbol{t}(\boldsymbol{x}_{s,i}):r\in(0,\Delta r]\}} s_1(\boldsymbol{x}), \tag{D.7}$$

for small $\Delta r > 0$. In practice, we approximate this search by selecting the adjacent grid point with the largest gradient magnitude in the quadrant indicated by the local tangent to the current grid point. The step length is therefore at most one grid diagonal, and we do not prescribe Δr. Repeating this procedure until the tracing terminates gives a curve that parameterizes the discontinuity location

$$\Gamma_N = \{\boldsymbol{x}_{s,i}\}_{i=0}^N. \tag{D.8}$$

Tracing terminates when the next selected grid point has already been visited, which is not necessarily the starting point.

Appendix D.2. Identifying Smooth State Extensions for a Scalar Field

For 2D scalar fields, we obtain smooth, globally defined, state extensions by applying the 1D optimization methodology described in Appendix C.3 locally normal to the curve Γ. Given a point $\boldsymbol{x}_{s,i} \in \Gamma$, we compute the normal vector

$$\boldsymbol{n}(\boldsymbol{x}_{s,i}) = \frac{1}{\|\nabla f(\boldsymbol{x}_{s,i})\|_2}\begin{bmatrix}\partial_x f(\boldsymbol{x}_{s,i})\\ \partial_y f(\boldsymbol{x}_{s,i})\end{bmatrix}. \tag{D.9}$$

We then define the line passing through $\boldsymbol{x}_{s,i}$ in the normal direction,

$$\boldsymbol{l}_i(\eta) = \boldsymbol{x}_{s,i} + \eta\boldsymbol{n}(\boldsymbol{x}_{s,i}), \tag{D.10}$$

where $\eta \in \mathbb{R}$ denotes the signed distance from $\boldsymbol{x}_{s,i}$ along the normal direction. Restricting the solution to this line yields the 1D profile

$$f_i(\eta) = f(\boldsymbol{x}_{s,i} + \eta \boldsymbol{n}(\boldsymbol{x}_{s,i})), \tag{D.11}$$

to which we apply the 1D fitting procedure described in Appendix C.3. We additionally compute the local level set function along $\boldsymbol{l}_i$ as

$$\varphi_i(\eta) = \eta. \tag{D.12}$$

Repeating this procedure for every $i = 1, \ldots, N$ yields a set of curves locally normal to the discontinuity. We compute global functions by interpolating using radial basis functions.

Appendix D.3. Level Set Representation for the 2D Euler Equations

To construct a level set representation for a solution to the Euler equations, we apply the methodologies developed in Appendix D.1 and Appendix D.2 directly to the density and pressure fields. For the velocity field, we identify the zero level set by applying the procedure outlined in Appendix D.1 to the norm of the velocity field $\|\boldsymbol{u}\|$. To compute the state extensions, we decompose the velocity field into its normal and tangential components

$$u_n = \boldsymbol{u} \cdot \boldsymbol{n}, \qquad u_t = \boldsymbol{u} \cdot \boldsymbol{t}, \tag{D.13}$$

where $\boldsymbol{n}$ and $\boldsymbol{t}$ denote the unit normal and tangent vectors, respectively. We then apply the methodology from Appendix D.2 to u_n, obtaining a level set representation of the normal velocity component. The level set representations of the Cartesian velocity components are subsequently recovered using u_t and the level set representation of u_n:

$$u_k = u_{n,k} n_x - u_t n_y, \qquad v_k = u_{n,k} n_y + u_t n_x, \qquad k = 1, \ldots, N_d + 1, \tag{D.14}$$

where N_d denotes the number of discontinuities. Once we have fit the state extensions to u_n and u_t, we recover u and v using the above relations.

Appendix D.4. 2D Registration Process

This subsection introduces the 2D registration process. First we align the level set functions. Then, using information from this alignment, we align the state extensions corresponding to the rarefaction wave. Appendix D.4.1 introduces the procedure to align the level set functions, while Appendix D.4.2 introduces the procedure for the state extensions.

Appendix D.4.1. 2D Registration Process: Level Set Functions

Solutions to the 2D blast wave problem produce zero level sets that are circular, so we introduce the registration map

$$\mathcal{R}^{(2D)}_{(a^{(i)}, b^{(i)}, \boldsymbol{c}^{(i)}, \boldsymbol{c}^{(1)})}(\varphi^{(i)})(\boldsymbol{x}) = \varphi^{(i)} \left(\boldsymbol{c}^{(i)} + \frac{\|\boldsymbol{x} - \boldsymbol{c}^{(1)}\| - b^{(i)}}{a^{(i)} \|\boldsymbol{x} - \boldsymbol{c}^{(1)}\|} \left(\boldsymbol{x} - \boldsymbol{c}^{(1)} \right) \right) \tag{D.15}$$

which aligns the center of the zero level set of $\varphi^{(i)}$ to that of $\varphi^{(1)}$, while also scaling and shifting the radial coordinate. Here, $\boldsymbol{c}^{(i)}$ denotes the center of the zero level set for $\varphi^{(i)}$, while $a^{(i)}$ is a radial scaling parameter, and $b^{(i)}$ is a radial shift. We need only align the centers of the level set functions, so we set $a^{(i)} = 1$ and $b^{(i)} = 0$. We independently fit centers to the zero level set of each level set function, and subsequently evaluate the registration map $\mathcal{R}^{(2D)}_{(1,0,\boldsymbol{c}^{(i)},\boldsymbol{c}^{(1)})}(\varphi^{(i)})$ for $i = 2, \ldots, N_e$.

To estimate the center of a circle, we first note that, if a circle is centered at $\boldsymbol{c}^{(i)} = (c_x^{(i)}, c_y^{(i)})$ with radius $r^{(i)}$, then

$$(x - c_x^{(i)})^2 + (y - c_y^{(i)})^2 = (r^{(i)})^2, \tag{D.16a}$$

which can be rewritten as

$$x^2 + y^2 + dx + ey + f = 0, \tag{D.16b}$$

for

$$d = -2c_x^{(i)}, \quad e = -2c_y^{(i)}, \quad f = (c_x^{(i)})^2 + (c_y^{(i)})^2 + (r^{(i)})^2. \tag{D.16c}$$

We can then use D.16b to fit d, e, and f using linear least squares, and we recover the desired parameters as

$$c_x^{(i)} = -\frac{d}{2}, \quad c_y^{(i)} = -\frac{e}{2}, \quad r^{(i)} = \sqrt{\frac{d^2 + e^2}{2^2} - f}. \tag{D.16d}$$

We then use (D.15) with $a^{(i)} = 1$ and $b^{(i)} = 0$ to align the level set functions

Appendix D.4.2. Aligning the 2D State Extensions

Given the $\boldsymbol{c}^{(i)}$ from the level set function $\boldsymbol{\phi}^{(i)}$, corresponding, to the density field $\rho^{(i)}$, we align the density field $\rho^{(i)}$ to the density field $\rho^{(1)}$ by seeking $a^{(i)}$ and $b^{(i)}$ that minimizes the difference between the gradients of their solutions. We compute the solution gradients as

$$s^{(i)}(\boldsymbol{x}) = \sqrt{\frac{\partial \rho^{(i)}}{\partial x}^2 + \frac{\partial \rho^{(i)}}{\partial y}^2} \tag{D.17}$$

and normalize them As

$$s^{(i)*}(\boldsymbol{x}) = \frac{s^{(i)}(\boldsymbol{x})}{\max_{\boldsymbol{x} \in \mathcal{D}} s^{(i)}(\boldsymbol{x})}. \tag{D.18}$$

Then we solve the minimization problem

$$(a^{(i)}, b^{(i)}) = \underset{a \in \mathbb{R}_{>0}, b \in \mathbb{R}}{\arg\min} \, \| s^{(1)*}(\boldsymbol{x}) - \mathcal{R}^{(2\mathrm{D})}_{(a,b,\boldsymbol{c}^{(i)},\boldsymbol{c}^{(1)})}(s^{(i)*})(\boldsymbol{x}) \|_2^2. \tag{D.19}$$

This mimics the 1D procedure developed in Appendix C.6, but applied radially.